Chemical Engineering Journal 482 (2024) 148719

Contents lists available at ScienceDirect

Chemical Engineering Journal

journal homepage: www.elsevier.com/locate/cej

Detailed kinetic modeling of catalytic oxidative coupling of methane

Jaspreet Chawla [a], Sven Schardt [a], Patrick Lott [a], Sofia Angeli [a], Steffen Tischer [b], Lubow Maier [b], Olaf Deutschmann [a,b,*]

[a] Institute for Chemical Technology and Polymer Chemistry (ITCP), Karlsruhe Institute of Technology (KIT), D-76131 Karlsruhe, Germany
[b] Institute of Catalysis Research and Technology (IKFT), Karlsruhe Institute of Technology (KIT), D-76344 Eggenstein-Leopoldshafen, Germany

ARTICLE INFO

Keywords:
Oxidative coupling of methane
High temperature
Acetylene
Heterogeneous reactions
Homogenous reactions
Short contact reactors

ABSTRACT

The oxidative coupling of methane (OCM) at high temperature over monolithic Pt-based catalysts operated at short contact times is investigated as an attractive method for methane upgrading to higher value products like ethylene and acetylene. An experimental measurement campaign aiming at elucidating the effect of operation parameters on the catalyst performance revealed that lower N_2 dilution, lower CH_4/O_2 ratio, and higher space velocities promote high C_2 yields. A maximum C_2 yield of 10 % with 94 % CH_4 conversion was obtained at a CH_4/O_2 ratio of 1.1, 50 % N_2 dilution, and a space velocity of 4.5×10^5 h^{-1}. Since both heterogenous and homogenous gas-phase chemistry together are required for determining C_2 formation pathways, a detailed OCM surface reaction mechanism over Pt is presented consisting of 26 species and 86 reactions that are consistent from the view of thermodynamics and micro-kinetic reversibility. The combination of this OCM surface mechanism with a detailed gas-phase mechanism allows a numerical micro-kinetic description of the experimental measurements. The simulations presented in this study suggest that C_2 formation takes place in the gas-phase at temperature above 1200 K with both oxidative and pyrolytic pathways for methane dehydrogenation to form CH_3 radicals, whose coupling results in C_2H_6, C_2H_4 and C_2H_2 formation. Furthermore, the simultaneous presence of sufficient oxygen content and heat are vital for high C_2 species yields.

1. Introduction

Methane (CH_4) is an abundant feedstock that predominately originates from natural gas. Over the years, various technologies have been developed for the efficient utilization of CH_4 to syngas (mixtures of hydrogen (H_2) and carbon monoxide (CO)) [1–3], which can then be processed into chemicals and fuels using a wide range of technologies. Furthermore, several ways for upgrading the CH_4 component, such as oxidative coupling of methane (OCM) or non-oxidative coupling of methane (NOCM) have been investigated, thereby establishing technologies for C_2 species formation. Ethylene (C_2H_4) and acetylene (C_2H_2) are the most significant and basic building element in the petrochemical industry, hence its efficient manufacture is critical [4]. The NOCM gives a high selectivity towards C_2 products, but due to a limited CH_4 conversion, typically only small C_2 yields are produced [5,6]. In contrast, OCM allows for significant conversion of CH_4, but the selectivity towards C_2 is a relatively low, since high amounts of CO and carbon dioxide (CO_2) are formed during partial and total oxidation reactions [4,7–10].

In the 1990s, Schmidt and his team pioneered the use of foam or honeycomb substrates coated with a metal-containing washcoat to demonstrate the autothermal operation of the catalytic partial oxidation (CPOX) reformers on a lab scale [11–16]. Hickmann and Schmidt (1993) found that adding oxygen (O_2) to the methane feed allowed syngas to be generated over Rh-based catalysts [13]. In contrast, high amounts of C_2 species were generated when using the same reactor configuration with Pt-based catalysts [13,15,17]. Since the total oxidation reactions are exothermic, neither of these processes requires the addition of external heat and high temperature is autothermally achieved inside the reactor. The higher temperature due to higher water selectivity and lower H_2 selectivity observed over Pt than Rh is attributed to the difference in activation energy for the formation of OH radicals on the surface. A lower stability of OH radicals over the Rh surface favors the H_2 formation reaction, whereas H_2O formation is favored over Pt [14,18,19]. Comprehensive laboratory tests demonstrated that the conversion of methane in platinum-coated monolithic reactors can reach 90 % CH_4

* Corresponding author at: Institute for Chemical Technology and Polymer Chemistry (ITCP), Karlsruhe Institute of Technology (KIT), D-76131 Karlsruhe, Germany.
E-mail address: deutschmann@kit.edu (O. Deutschmann).

https://doi.org/10.1016/j.cej.2024.148719

Available online 13 January 2024

conversion with C_2 selectivity as high as 20 % at a space velocity of 1.5 $\times 10^5 h^{-1}$, atmospheric pressure, with a CH_4/O_2 ratio of 1.4 and 20 % N_2 dilution. Furthermore, a strong correlation of space velocity, N_2 dilution and input CH_4/O_2 ratio towards C_2 formation is visualized by experiments [17,20].

Several researchers have pursued detailed chemical kinetic modeling in order to elucidate CPOX of hydrocarbons over the Pt catalyst and a variety of pathways have been proposed [21–28]. It was investigated that methane CPOX over Pt foam catalysts is largely driven by kinetics [29]. According to earlier research on methane CPOX over Pt on ceramic foam monoliths, a limited zone at the entry of the catalyst foam is where total oxidation of methane takes place, followed by a partial oxidation zone leading to formation of CO and H_2 [29–31]. A prolonged endothermic steam reforming zone follows this oxidation zone, and at low enough catalyst temperatures, also a water gas shift reaction is observed. However, there is little impact from dry reforming [23,27,29].

In contrast to CPOX, the formation of C_2 species by means of OCM over Pt has not yet been comprehensively described by a detailed reaction mechanism that is capable of capturing both gas-phase and surface processes. Our previous research put forward that interplay of both heterogenous and homogenous chemistry, which together govern the C_2 species formation over Pt by OCM at extremely short contact times [32]. The catalyst was vital for oxidation of surface C and H species in order to generate localized heat that promotes endothermic homogeneous reactions [33]. Thus, the higher temperatures are further crucial for activation of non-catalytic processes in the gas-phase, for the creation of higher hydrocarbons. Furthermore, the formation of C_2 products was attributed to the formation of CH_3 radicals in the gas-phase, and CH_2 and CH radicals were disregarded as potential sources of C_2 species [34].

In the current work, the potential contributions of both heterogenous and homogenous chemistry to the OCM over a platinum catalyst is evaluated. Starting from a microkinetic model by Kahle et al. [28] (22 species, 58 reactions) that was originally developed for high temperature dry reforming of methane over Pt catalysts, the incorporation of H(s) and OH(s) assisted dehydrogenation processes results in new thermodynamically consistent OCM surface mechanism. The new OCM surface mechanism is based on the mean-field approximation and includes 26 chemical species and 86 chemical reactions. The application of sensitivity and path analysis helped to further simplify the heterogeneous mechanism defined. It has also been demonstrated that pathways using oxygenates like HCO(s) and CH_2O(s) contribute. Further, free-radical reactions can explain the gradual dehydrogenation of methane. CH_3 species formed in the gas-phase may undergo either pure or oxygen-supported pyrolysis. Thus, methane can be directly transformed into hydrocarbons at high temperatures by thermally induced coupling processes in the gas-phase. These gas-phase processes that ultimately result in C_2 formation via OCM were described by including a detailed microkinetic gas-phase mechanism that was originally developed by Appel, Bockhorn, Frenklach (ABF) in the context of hydrocarbon oxidation and pyrolysis [35].

This study presents a comprehensive OCM microkinetic model on platinum that is thermodynamically consistent and is validated to a wide range of experimental conditions. Furthermore, the current work expands previous studies by providing insights on the complex interplay of gas-phase and heterogenous catalytic chemistry and covering a broad variation of reaction conditions in terms of (i) residence times, (ii) input fuel dilutions through N_2, and (iii) CH_4/O_2 ratio.

2. Experimental methods

A 1 wt-% Pt/γ-Al_2O_3 powder catalyst was prepared by incipient wetness impregnation as previously explained in detail by Chawla et al. [32], and thereafter coated onto a cylindrical cordierite honeycomb monolith (length 0.01 m, diameter 0.01 m, Corning) with a cell density of 400 cpsi (cells per square inch by the methodology adopted by Karinshak et al. [36]. Herein, the honeycomb geometry was chosen because back-pressure is only of minor concern. This is of particular relevance because the catalytic converters need to be operated with high flow velocities in order to ensure millisecond residence times that are considered a prerequisite for OCM.

The experimental setup used for catalytic testing, which is described in detail in our previous publication [32], includes a quartz glass tubular reactor with a length of 0.625 m that was used to house the monolithic catalyst. An inert honeycomb monolith (length = 0.01 m, diameter = 0.01 m) serving as heat shield was positioned 0.005 m in front of the catalyst to enhance the heat transfer. The reactor is placed inside a Carbolite HST 12/400 furnace, which was heated to 773 K during the catalyst tests. Before entering the reactor, the reaction gases N_2, CH_4, and O_2 are preheated to 463 K and mixed using mass flow controllers (Bronkhorst). The temperature of the exhaust gas is continuously monitored by a type S thermocouple located 0.005 m downstream of the catalyst while an online Fourier-transform infrared (FTIR) spectrometer (MultiGas 2030, MKS Instruments) analyzes the effluent gas stream composition of the exhaust gas.

The experiments for model development and validation were conducted with the monolithic Pt/Al_2O_3 catalyst described above at varying inlet reactor parameters; namely N_2 dilution, CH_4/O_2 ratio, space velocity. Table 1 lists the reactor conditions at which experiments were conducted with the monolithic 1 wt-% Pt/γ-Al_2O_3 sample (length = 0.01 m, diameter = 0.01 m, 400 cpsi) at an inlet temperature of 773 K. In contrast to the surface chemistry, which is restricted to the reactor section containing the monolithic catalyst sample, active gas-phase chemistry is considered both over the catalytic monolith and in the tubular reactor up to 0.40 m after the catalyst.

3. Modeling approach

3.1. Channel model

The processes during the operation of catalysts reactors can be predicted using multiscale modeling, commencing with the atomic-scale reaction mechanism, and adsorption and diffusion operations over the catalyst surface, as well as reaction rates on the surface and in the gas-phase [37,38]. This study uses elementary-step based kinetic models of gas-phase and surface reactions to couple the 2D DETCHEM^{CHANNEL} [39] reactor model simulations under reaction conditions of the chemical system. In order to account for heat transfer effects during catalyst operation at the given reaction conditions, DETCHEM^{MONOLITH} [40] simulations are performed for a honeycomb catalyst. Using the DETCHEM^{CHANNEL} [39] code, DETCHEM^{MONOLITH} [40] comprehensively simulates representative channels to model the transient temperature.

Schwiedernoch et al. [39] have provided thorough documentation of the modeling methodology for a channel reactor system, and our earlier investigations [32] have also provided summaries of the equations. Furthermore, the mean-field approximation is used to model the catalytic surface; thereby, the surface is made up of coverages with adsorbed species, which varies with temperature and the axial position within a channel. Calculations for surface coverages, kinetics, and production rates of surface reactions are also described in detail in Chawla et al. [32].

Table 1
Reactor conditions chosen for the experiments with the monolithic 1 wt-% Pt in γ-Al_2O_3 sample (length = 0.01 m, diameter = 0.01 m, 400 cpsi) at inlet temperature of 773 K.

Parameter	GHSV variation	N_2 variation	CH_4/O_2 variation
GHSV ($\times 10^5 h^{-1}$)	2.9–6.2	2.9	4.5
CH_4/O_2 molar ratio	1.1	1.1	1.1–2.0
N_2 dilution (%)	50	50–70	50

3.2. Thermodynamic consistency

The ability to accurately anticipate the thermodynamic equilibrium in the limit of infinite time is one of the prerequisites of a micro-kinetic model. Therefore, it is important to ensure that each elementary reaction is micro-kinetically reversible. Using the methodology adopted by Herrera Delgado et al. [41] for a reversible reaction (Eq. (1), the thermodynamic consistency establishes a dependence between the rate parameters of the forward and reverse reactions using Eqs. (2) and (3):

$$\sum_{i=1}^{N_g+N_s} \nu'_{ij} A_i \underset{k_r}{\overset{k_f}{\rightleftarrows}} \sum_{i=1}^{N_g+N_s} \nu''_{ij} A_i \tag{1}$$

$$\frac{k_f(T)}{k_r(T)} = F_{c/p} \exp\left(-\frac{\Delta_R G(T)}{RT}\right) \tag{2}$$

$$F_{c/p} = \frac{K_c(T)}{K_p(T)} = \prod_{i=1}^{N_g+N_s} (c_i^{\Theta})^{\nu_i} \tag{3}$$

Here, A_i represents the i^{th} species with ν'_{ij} and ν''_{ij} denoting as the stoichiometric coefficients for the reactants and products in the reaction respectively, N_g is the number of gas-phase species, N_s is the number of surface species. The equilibrium is described by the equilibrium constant $K_p(T) = \exp\left(-\frac{\Delta_R G(T)}{RT}\right)$, which needs to be converted into a constant with respect to concentrations $K_c(T)$ by Eq. (3). $\Delta_R G(T)$ is the change of Gibbs free energy in the reaction and R is the universal gas constant. c_i^{Θ} depicts the species concentration under standard pressure, $c_i^{\Theta} = \frac{p^{\Theta}}{RT}$ for ideal gaseous species and $c_i^{\Theta} = \frac{\Gamma}{\sigma_i}$ for surface species. Where, σ_i denotes the number of sites occupied by a particle of species i and Γ represents the surface site density of the surface.

Note, that all reactions of a reaction mechanism must fulfill Eq. (2) in order to be deemed thermodynamically consistent for the range of temperature considered.

3.3. Reaction flow analysis

Based on the rate of species generation, a reaction flow analysis (RFA) identifies and defines the main sequential paths for the formation of products and consumption of reactants in a chemical reaction mechanism. The approach used in this study was taken from Gossler et al. [41]. The integral RFA determines which reactions contributed the most over the time period under consideration by integrating the reaction rates over all the reaction processes. Therefore, the effective reaction rate, which accounts for the forward and reverse directions of the reactions and determines the contribution of a specific reaction to the formation of a chemical species, is given by the following Eq. (4).

$$r_{eff,j} = k_f \prod_{i=1}^{N_g+N_s} c_i^{\nu'_{ij}} - k_r \prod_{i=1}^{N_g+N_s} c_i^{\nu''_{ij}} \tag{4}$$

The desired form, expressed in mol units, is produced by multiplying the aforementioned equation by the volume. A negative value indicates that the reaction is actually moving the backward direction.

3.4. Chemical reaction system

3.4.1. The gas-phase chemistry

For the present study, we adopted a detailed chemical gas-phase mechanism that was originally established by Appel, Bockhorn, and Frenklach (ABF) [35], which includes 99 chemical species and 543 reactions. The ABF mechanism is capable of describing the formation of hydrocarbons up to C_6 species and aromatics and has already been proven being well-suited under a variety of homogeneous gas-phase circumstances, such as both pyrolytic and oxidative conversion of C_1 and C_2 species and also under the autoignition conditions [42–44]. Note, that for the present study the thermochemical and transport data corresponding to the gas-phase chemistry was used without modification.

3.4.2. The surface chemistry

A mechanism with 22 species and 58 reactions that was originally developed by Kahle et al. [28] for dry reforming of methane over Pt pellets with an equimolar feed composition of CH_4 and CO_2 at high temperature (1123–1273 K) and at high pressure (up to 20 bar) served as starting point for the description of the surface chemistry during OCM. Since the original dry reforming mechanism does not include C_2 formation pathways, the detailed reaction mechanism by Kahle et al. [28] was extended as described in section 4.3.

3.5. Modeling methodology

The reaction network is highly sensitive to temperature, which further impacts the reaction rates, reaction conditions, and species composition, i.e. conversion of reactants and formation of products. The modeling methodology adopted in this study is described in schematic Fig. 1. The operational approach used for the modeling of the experimental data involved the initial phase of establishing the temperature profiles under reactor conditions using the 2D transient single channel simulations, inclusion of heat transport effects with axial heat conduction and active surface chemistry only in the zone of the monolithic catalyst. In the current system, axial heat conduction was considered a crucial factor for establishment of determination of temperature rise inside the coated catalyst and is discussed in detail in the section 4.1. Thereafter, the temperature profile obtained is established as the input wall temperature profile to conduct further 2D steady-state single channel simulations with active both gas-phase and surface chemistry over the catalytic monolith.

The two-stage modeling method was adopted in the study due to lack of spatial temperature data for the experimental conditions considered due to measurement constraints. The first 2D transient single channel simulations were conducted using the above-described methodology under consideration of a channel length of 0.02 m and an empty zone of 0.005 m both at the entrance and exit of the coated catalyst. Given the high space velocity considered during experiments and high temperatures (more than 1300 K, in all cases) obtained, the residence time over the catalyst of only 1–4 ms is extremely short. Hence, an adiabatic system with heat conduction along the length is considered in the 2D transient single channel simulations. Due to the high computational time involved in the calculations, only surface reactions have been considered in the 2D transient single channel simulations. However, once the temperature profile has been determined from the first stage simulations, both active surface and gas-phase chemistry are taken into account as the 2D steady-state single channel simulations are carried out in order to get the required product distribution.

4. Results and discussion

4.1. Description of the temperature profile

During OCM, the temperature is a decisive factor that strongly influences the evolution of product species [32,34]. Fig. 2 depicts the experimental temperature curve (dotted curve) obtained when operating the Pt/Al_2O_3 catalyst at $CH_4/O_2 = 1.1$, $N_2 = 50$ %, p = 1 bar, GHSV = 4.5×10^5 h^{-1}. In the short empty space between the heat shield and the catalytic monolith, an exponential temperature increase was seen prior to the entrance of the catalyst monolith, which can be explained by thermal conduction of the reaction heat evolving from catalytic CH_4 conversion. The temperature continues to rise until it

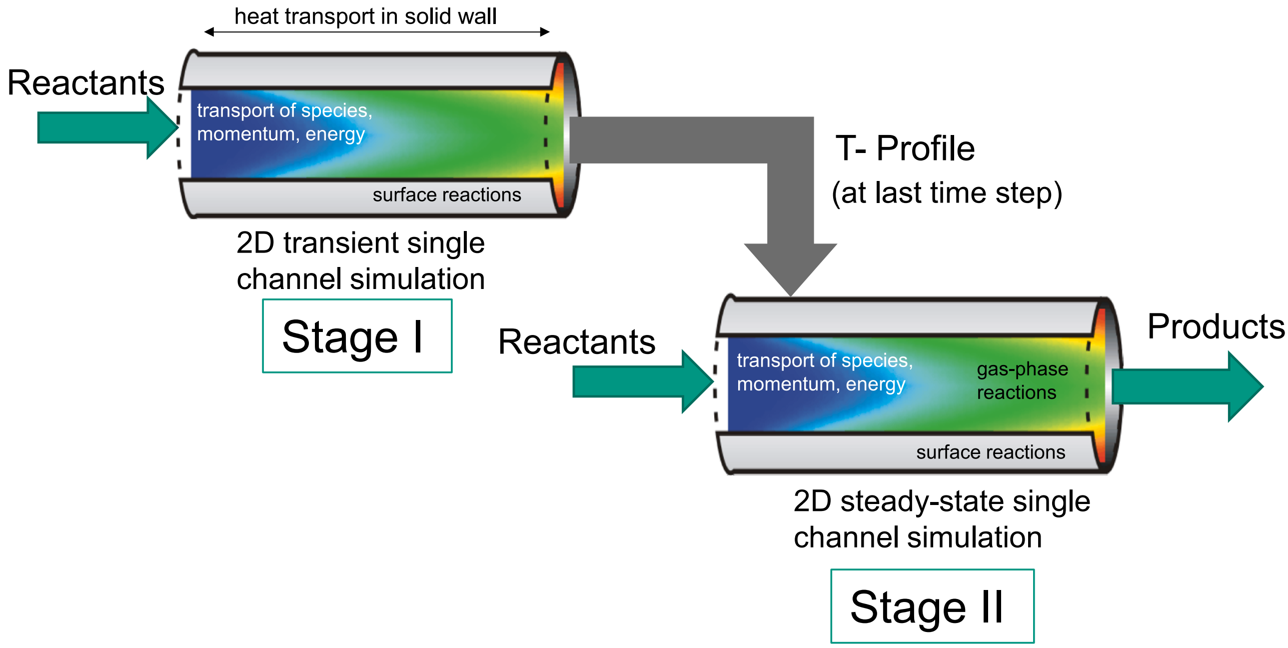

Fig. 1. Modeling methodology.

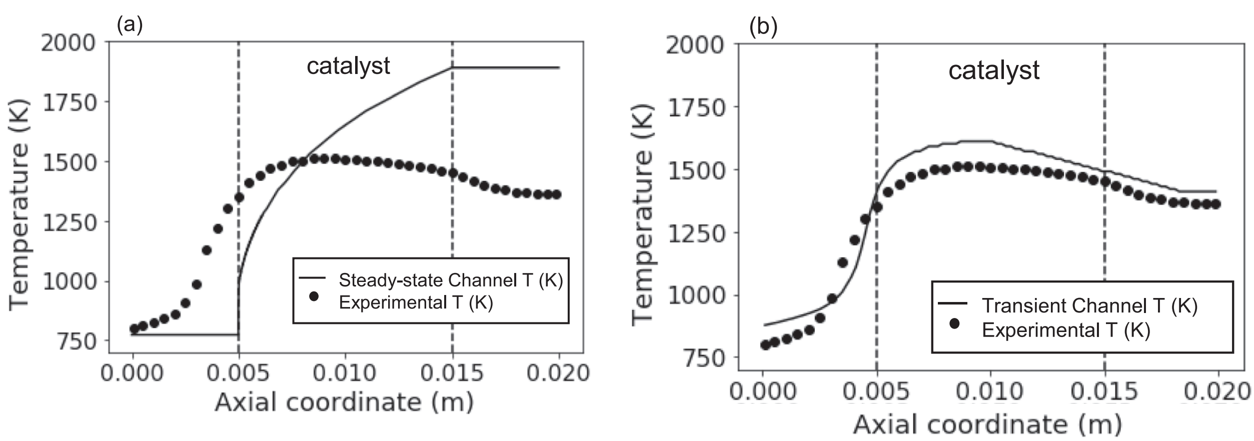

Fig. 2. Comparison of simulated (lines) and measured (points) temperature profile at $CH_4/O_2 = 1.1$, p = 1 bar, 50 % N_2, GHSV = 4.5×10^5 h^{-1}, (a) 2D steady-state single channel simulations (b) 2D transient single channel simulation.

reaches a peak temperature of 1550 K inside the Pt catalyst and then drops at the output.

The assumption of adiabatic conditions and the exclusive consideration of surface chemistry (gas-phase chemistry is not considered), the 2D steady-state single channel simulations surface mechanism does not yield a temperature increase before to the catalytic monolith (Fig. 2***(a)***). Instead, the temperature rises exponentially inside the catalyst before reaching a maximum temperature of 1900 K at the catalytic monolith's end, which is an overestimation of the experimentally determined maximum temperature. Hence, adiabatic 2D steady-state single channel simulations do not describe the system.

Therefore, 2D transient single channel simulations are conducted that allow an axial heat transfer along the solid wall of the catalytic monolith and 0.005 m up- and downstream of the coated catalyst. As depicted in Fig. 2***(b)***, the consideration of axial transfer of the reaction heat that is generated by the catalytic CH_4 conversion over platinum results in a simulated temperature profile that adequately mimics the temperature profile measured in the experimental setup. A pronounced temperature increases prior to the catalyst, a maximum in the monolith, and a moderate decline downstream the catalyst.

In order to validate the approach for temperature profile simulations, further operation points at varying space velocities (GHSV = 2.9–6.2 $\times$ 10^5 h^{-1}) and reaction conditions ($CH_4/O_2 = 1.0$, N_2 = 50 %, p = 1 bar) were simulated. As shown in Fig. 3, the 2D transient single channel simulations predict the temperature that was measured 0.005 m downstream of the catalytic monolith rather well. Notably, these results point to a strong influence of axial heat conduction along the reactor. Thus, the transient single channel simulations with axial conduction are important in determination of temperature profile developed inside the reactor for all the measured input reactor conditions. Due to high temperature achieved inside the catalytic reactor, experimental measurement of temperature profile was not always feasible. With the application of 2D transient channel simulations, the T-profile suggested in Stage I of the methodology in Fig. 1, was kinetically modelled. Thereafter, the temperature profile obtained is further employed as wall temperature for 2D steady-state single channel simulations (Stage II, Fig. 1) with both active surface and gas-phase chemistry over the coated catalyst monolith, determinant for the product gas distribution.

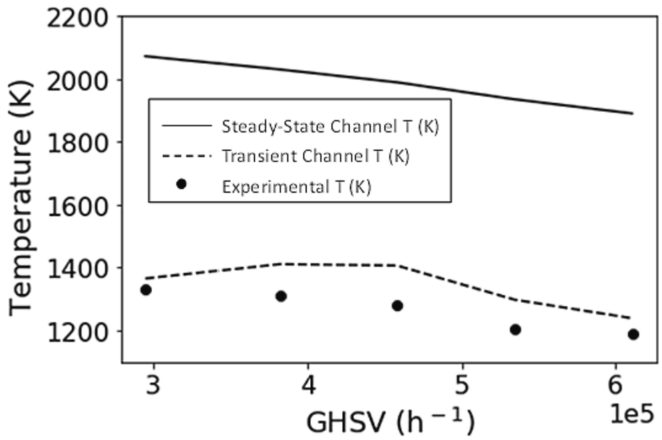

Fig. 3. Comparison of experimental and modeled gas temperature at 0.005 m downstream of the catalytic monolith for variation in space velocity (2D transient single channel simulation: Dashed line and 2D steady-state single channel simulations: Solid line).

4.2. Modeling with mechanisms from literature: Surface and gas-phase chemistry

The first 2D steady-state single channel simulations were conducted using the methodology described in section 3.5, considering both surface kinetic model (Kahle et al. [28]) and gas-phase chemistry (ABF mechanism [35]) over the catalyst sample. The kinetic simulations were run across a reactor length of 0.4 m, simultaneously considering surface and gas-phase chemistry over the monolithic 1 wt−% Pt/Al_2O_3 catalyst with a noble metal loading of 30 g/ft^3 (0.01 m), whereas only gas-phase chemistry was considered in the empty (0.39 m) quartz glass tubular reactor downstream of the monolith. The conversion and yield of the products are calculated based on the initial methane content in the feed gas stream.

The experimental measurement campaign that varies the GHSV from $2.9-6.2\times10^5$ h^{-1} with reaction conditions of $CH_4/O_2 = 1.1$, $N_2 = 50$ %, p = 1 bar was shows that the C_2 yield initially plateaus with rising space velocity and subsequently tends to drop as the space velocity increases beyond 4.5×10^5 h^{-1} (Fig. 4). In addition, methane conversion decreases with rising space velocity, and a larger decrease was observed once the space velocity exceeds 4.5×10^5 h^{-1}, which may also contribute to the decline in C_2 yields.

As shown in Fig. 4, the channel simulations describe the temperature at the catalyst outlet, CH_4 conversion and CO_x formation fairly well. However, the C_2 species, which are in the focus of this study, were highly underpredicted, and particularly C_2H_2, which is the main product among the C_2 species in our experiments, appears to be insignificant according to the simulations. These discrepancies call for a major modification of the reaction mechanism in order to improve the description of the C-C coupling chemistry that that is capable of capturing the formation of C_2 hydrocarbons. In this regard, the inclusion of additional species and reaction pathways allows for a sufficient consideration of the complex interactions between gas-phase and surface chemistry, which is considered crucial in the context of OCM [32,34].

4.3. Extending the surface reaction mechanism

For modifying the existing surface mechanism, a detailed surface chemistry with 35 adsorbed chemical species and 283 reversible reactions that was developed by Vincent et al. [24] for describing the production of ethylene through dehydrogenation of ethane over a short contact time ceramic foam catalyst coated with Pt/Al_2O_3 was studied. Notably, the mechanism was developed by establishing activation energy barriers, reaction enthalpy changes, and temperatures of adsorption of adsorbed species for all essential steps of the process by means of density functional theory (DFT) and the unity bond index-quadratic exponential potential (UBI-QEP) approach. By adding 4 new species and 14 reversible reactions that describe oxygenate decomposition and their interaction with H, OH, O radicals over the Pt surface from the mechanism developed by Vincent et al. [24], the original reaction scheme by Kahle et al. [28] was extended for our present study on OCM. Moreover, since earlier research provides strong evidence for CH_3 radical coupling over the surface as an additional reaction pathway during OCM [21,24,45], CH_3 radical coupling was not only considered in the gas-phase but also on the surface to form C_2H_6 [24]. Furthermore, Zhu et al. also discussed the presence of CHx coupling over noble metal catalyst via ab initio DFT calculations [46]. To ensure the microkinetic reversibility of each elementary step upon addition of new reactions, the thermodynamic consistency of the new OCM surface mechanism was maintained following the procedure given in section 3.2. Thereby, all species in the resulting mechanism exhibit thermodynamic functions that depend accurately on temperature in the range of 773–2000 K. The newly proposed, thermodynamically consistent OCM surface mechanism, that was established and validated using multiple sets of experiments for OCM over a Pt/Al_2O_3 monolith catalyst, is given in Table 2. Through sequential iterative comparisons of numerically predicted and experimentally determined species concentrations, the predictive behavior of the overall reactor model for OCM was evaluated.

Consequently, the newly proposed OCM surface model comprises 26 species and 86 reactions and incorporates HCO and CH_2O radical formation on the surface and their interactions with H, O, and OH radicals over the Pt surface. The adsorption of CH_2O radicals on the surface and their further catalytic transformation to HCO is well supported in literature [24,26,47]. Furthermore, CH_2O adsorption on the surface and

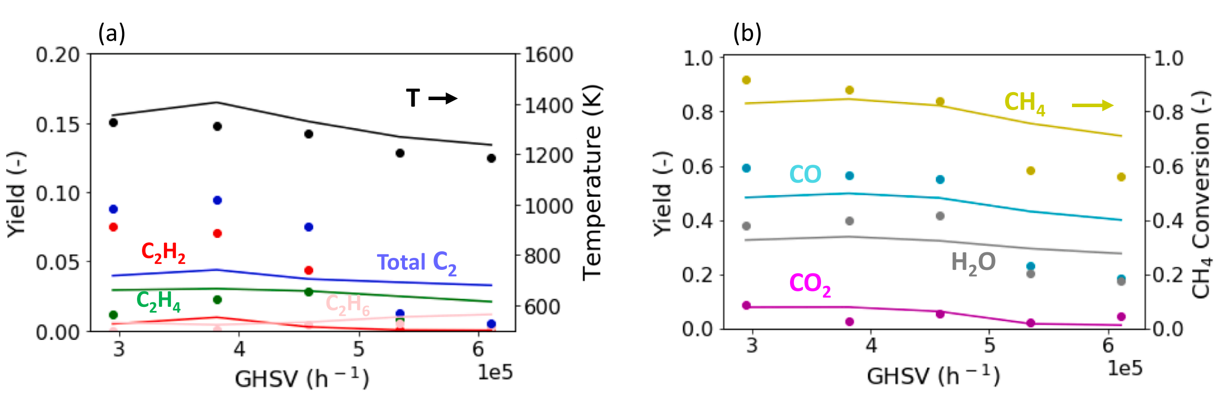

Fig. 4. Comparison of simulated (lines) and measured (points) for the influence of GHSV ($CH_4/O_2 = 1.1$, p = 1 bar, 50 % N_2), (a) yield of C_2 species and temperature downstream of monolith (b) CH_4 conversion, yield of CO_x and H_2O species.

Table 2
Heterogenous pathways involved in OCM over a Pt/Al_2O_3 catalyst.

	Reaction	A(cm, mol, s) / S_0	β	E_a (kJ/mol)	$\epsilon_{ik}\theta_i$
R 1	$Pt(s) + Pt(s) + O_2 \rightarrow O(s) + O(s)$	6.71E-05	−0.15	−1.55	
R 2	$O(s) + O(s) \rightarrow Pt(s) + Pt(s) + O_2$	3.03E + 19	0.67	233.64	$+15.65\theta_O$
R 3	$H_2 + Pt(s) + Pt(s) \rightarrow H(s) + H(s)$	2.91E-04	0.08	−15.37	
R 4	$H(s) + H(s) \rightarrow H_2 + Pt(s) + Pt(s)$	4.40E + 21	−0.16	60.52	$+4.45\theta_H$
R 5	$Pt(s) + H_2O \rightarrow H_2O(s)$	1.94E-01	0.00	8.61	
R 6	$H_2O(s) \rightarrow Pt(s) + H_2O$	5.30E + 15	−0.18	53.72	$+33.00\theta_{CO}$
R 7	$Pt(s) + OH \rightarrow OH(s)$	5.15E-01	−0.02	1.22	
R 8	$OH(s) \rightarrow Pt(s) + OH$	1.01E + 17	0.10	246.00	
R 9	$Pt(s) + CO \rightarrow CO(s)$	5.21E-01	0.02	3.46	
R 10	$CO(s) \rightarrow Pt(s) + CO$	2.67E + 16	−0.41	144.45	$+36.30\theta_{CO}$ $+4.29\theta_H$ $+6.00\theta_{H2O}$
R 11	$Pt(s) + CO_2 \rightarrow CO_2(s)$	9.82E-02	−0.06	3.15	$+86.32\theta_O$
R 12	$CO_2(s) \rightarrow Pt(s) + CO_2$	4.29E + 12	0.53	10.80	$+8.18\theta_{CO}$
R 13	$Pt(s) + Pt(s) + CH_4 \rightarrow H(s) + CH_3(s)$	8.20E-04	0.03	11.82	
R 14	$H(s) + CH_3(s) \rightarrow Pt(s) + Pt(s) + CH_4$	3.69E + 25	−0.17	3.17	$+2.23\theta_H$
R 15	$Pt(s) + CH_4 + O(s) \rightarrow OH(s) + CH_3(s)$	5.96E + 15	0.69	43.75	$+7.82\theta_O$
R 16	$OH(s) + CH_3(s) \rightarrow Pt(s) + CH_4 + O(s)$	3.11E + 24	0.02	86.15	
R 17	$OH(s) + CH_4 + Pt(s) \rightarrow H_2O(s) + CH_3(s)$	2.84E-01	0.05	23.18	
R 18	$H_2O(s) + CH_3(s) \rightarrow OH(s) + CH_4 + Pt(s)$	1.93E + 26	−0.19	57.90	$+33.00\theta_{CO}$
R 19	$CO(s) + O(s) \rightarrow Pt(s) + CO_2(s)$	3.67E + 21	0.08	113.88	$+28.13\theta_{CO}$ $+4.29\theta_H$ $+6.00\theta_{H2O}$
R 20	$Pt(s) + CO_2(s) \rightarrow CO(s) + O(s)$	1.17E + 22	−0.08	149.73	$-94.14\theta_O$
R 21	$OH(s) + CO(s) \rightarrow Pt(s) + COOH(s)$	2.69E + 12	0.04	42.74	$+36.30\theta_{CO}$ $+4.29\theta_H$ $+6.00\theta_{H2O}$
R 22	$Pt(s) + COOH(s) \rightarrow OH(s) + CO(s)$	8.71E + 11	−0.04	25.91	
R 23	$Pt(s) + COOH(s) \rightarrow H(s) + CO_2(s)$	4.71E + 11	0.05	50.65	$+86.32\theta_O$
R 24	$H(s) + CO_2(s) \rightarrow Pt(s) + COOH(s)$	3.26E + 12	−0.05	52.28	$+8.18\theta_{CO}$ $+2.23\theta_H$
R 25	$H(s) + COOH(s) \rightarrow CO(s) + H_2O(s)$	1.15E + 13	−0.02	28.08	
R 26	$CO(s) + H_2O(s) \rightarrow H(s) + COOH(s)$	5.38E + 11	0.02	88.28	$+69.30\theta_{CO}$ $+2.06\theta_H$ $+6.00\theta_{H2O}$
R 27	$C(s) + CO_2(s) \rightarrow CO(s) + CO(s)$	4.47E + 19	−0.01	−5.57	
R 28	$CO(s) + CO(s) \rightarrow C(s) + CO_2(s)$	8.27E + 17	0.01	210.00	$+86.32\theta_O$ $+64.43\theta_{CO}$ $+8.57\theta_H$ $+12.00\theta_{H2O}$
R 29	$Pt(s) + CH_3(s) \rightarrow CH_2(s) + H(s)$	6.73E + 22	0.04	69.76	
R 30	$CH_2(s) + H(s) \rightarrow Pt(s) + CH_3(s)$	5.80E + 21	−0.04	0.54	$+2.23\theta_H$
R 31	$CH_2(s) + Pt(s) \rightarrow CH(s) + H(s)$	1.16E + 23	0.04	37.54	
R 32	$CH(s) + H(s) \rightarrow CH_2(s) + Pt(s)$	1.94E + 22	−0.04	21.36	$+2.23\theta_H$
R 33	$Pt(s) + CH(s) \rightarrow C(s) + H(s)$	2.14E + 22	0.04	48.55	$-2.23\theta_H$
R 34	$C(s) + H(s) \rightarrow Pt(s) + CH(s)$	1.80E + 22	−0.04	89.45	
R 35	$H(s) + O(s) \rightarrow OH(s) + Pt(s)$	2.58E + 21	−0.01	18.72	$+2.23\theta_H$
R 36	$OH(s) + Pt(s) \rightarrow H(s) + O(s)$	3.67E + 21	0.01	69.78	$-7.82\theta_O$
R 37	$OH(s) + H(s) \rightarrow Pt(s) + H_2O(s)$	1.76E + 23	0.02	3.46	$+2.23\theta_H$
R 38	$Pt(s) + H_2O(s) \rightarrow OH(s) + H(s)$	2.66E + 21	−0.02	46.84	$+33.00\theta_{CO}$
R 39	$OH(s) + OH(s) \rightarrow H_2O(s) + O(s)$	2.64E + 21	0.03	62.39	
R 40	$H_2O(s) + O(s) \rightarrow OH(s) + OH(s)$	2.81E + 19	−0.03	54.71	$+7.82\theta_O$ $+33.00\theta_{CO}$
R 41	$C(s) + O(s) \rightarrow Pt(s) + CO(s)$	1.53E + 20	0.07	−7.46	$+7.82\theta_O$ $-36.30\theta_{CO}$
R 42	$Pt(s) + CO(s) \rightarrow C(s) + O(s)$	8.98E + 18	−0.07	243.96	$+4.29\theta_H$ $+6.00\theta_{H2O}$
R 43	$CH_3(s) + O(s) \rightarrow CH_2(s) + OH(s)$	3.73E + 23	0.03	85.95	$+7.82\theta_O$
R 44	$CH_2(s) + OH(s) \rightarrow CH_3(s) + O(s)$	4.57E + 22	−0.03	67.78	
R 45	$CH_2(s) + O(s) \rightarrow OH(s) + CH(s)$	1.51E + 24	0.03	69.50	$+7.82\theta_O$
R 46	$OH(s) + CH(s) \rightarrow CH_2(s) + O(s)$	3.58E + 23	−0.03	104.38	
R 47	$CH(s) + O(s) \rightarrow OH(s) + C(s)$	2.24E + 21	0.03	42.37	$+7.82\theta_O$
R 48	$OH(s) + C(s) \rightarrow CH(s) + O(s)$	2.69E + 21	−0.03	134.34	
R 49	$OH(s) + CO(s) \rightarrow H(s) + CO_2(s)$	6.68E + 20	0.09	29.15	$+86.32\theta_O$ $+28.13\theta_{CO}$ $+2.06\theta_H$ $+6.00\theta_{H2O}$
R 50	$H(s) + CO_2(s) \rightarrow OH(s) + CO(s)$	1.50E + 21	−0.09	13.95	
R 51	$H_2O(s) + C(s) \rightarrow OH(s) + CH(s)$	1.31E + 19	−0.07	136.13	$+33.00\theta_{CO}$
R 52	$OH(s) + CH(s) \rightarrow H_2O(s) + C(s)$	1.03E + 21	0.07	51.85	
R 53	$CH(s) + H_2O(s) \rightarrow CH_2(s) + OH(s)$	9.63E + 17	−0.07	91.69	$+33.00\theta_{CO}$
R 54	$CH_2(s) + OH(s) \rightarrow CH(s) + H_2O(s)$	3.82E + 20	0.07	64.48	
R 55	$CH_2(s) + H_2O(s) \rightarrow OH(s) + CH_3(s)$	1.33E + 18	−0.07	42.34	$+33.00\theta_{CO}$
R 56	$OH(s) + CH_3(s) \rightarrow CH_2(s) + H_2O(s)$	1.02E + 21	0.07	68.19	

(*continued on next page*)

Table 2 (*continued*)

	Reaction	A(cm, mol, s) / S_0	β	E_a (kJ/mol)	$\epsilon_{ik}\theta_i$
R 57	$OH(s) + C(s) \rightarrow CO(s) + H(s)$	7.24E + 18	0.08	−14.98	
R 58	$CO(s) + H(s) \rightarrow OH(s) + C(s)$	2.99E + 17	−0.08	185.38	$+36.30\theta_{CO}$ $+6.51\theta_{H}$ $+6.00\theta_{H2O}$
R 59	$Pt(s) + HCO \rightarrow HCO(s)$	4.02E + 04	0.69	−9.24	
R 60	$HCO(s) \rightarrow Pt(s) + HCO$	1.27E + 11	0.81	176.34	
R 61	$OH(s) + CO + Pt(s) \rightarrow HCO(s) + O(s)$	2.35E + 09	0.61	79.65	
R 62	$HCO(s) + O(s) \rightarrow OH(s) + CO + Pt(s)$	2.40E + 15	0.39	27.35	$+7.82\theta_{O}$
R 63	$HCO(s) + H(s) \rightarrow Pt(s) + H_2(s) + CO$	5.04E + 15	0.50	35.80	$+2.23\theta_{H}$
R 64	$Pt(s) + H_2(s) + CO \rightarrow HCO(s) + H(s)$	2.53E + 09	0.50	0.00	
R 65	$Pt(s) + CO + CH_2O(s) \rightarrow HCO(s) + HCO(s)$	1.43E + 10	0.58	7.51	
R 66	$HCO(s) + HCO(s) \rightarrow Pt(s) + CO + CH_2O(s)$	6.59E + 14	0.42	18.09	
R 67	$Pt(s) + H_2O(s) + CO \rightarrow HCO(s) + OH(s)$	2.63E + 08	0.58	58.91	$+33.00\theta_{CO}$
R 68	$HCO(s) + OH(s) \rightarrow Pt(s) + H_2O(s) + CO$	2.52E + 16	0.42	14.29	
R 69	$CH_2O + Pt(s) + O(s) \rightarrow HCO(s) + OH(s)$	2.29E + 09	0.41	0.63	$+7.82\theta_{O}$
R 70	$HCO(s) + OH(s) \rightarrow CH_2O + Pt(s) + O(s)$	2.38E + 15	0.59	120.07	
R 71	$CH_2O + Pt(s) + OH(s) \rightarrow HCO(s) + H_2O(s)$	1.46E + 13	0.44	−10.73	
R 72	$HCO(s) + H_2O(s) \rightarrow CH_2O + Pt(s) + OH(s)$	1.62E + 17	0.56	101.03	$+33.00\theta_{CO}$
R 73	$CH_2O + Pt(s) + Pt(s) \rightarrow HCO(s) + H(s)$	7.38E + 08	0.42	−5.09	
R 74	$HCO(s) + H(s) \rightarrow CH_2O + Pt(s) + Pt(s)$	5.41E + 14	0.58	63.29	$+2.23\theta_{H}$
R 75	$CH_3(s) + O(s) \rightarrow CH_2O + H(s) + Pt(s)$	7.82E + 15	0.42	35.60	$+7.82\theta_{O}$
R 76	$CH_2O + H(s) + Pt(s) \rightarrow CH_3(s) + O(s)$	5.45E + 07	0.59	31.90	$+2.23\theta_{H}$
R 77	$CH_3(s) + O(s) \rightarrow H(s) + CH_2O(s)$	4.29E + 15	0.35	30.66	$+7.82\theta_{O}$
R 78	$H(s) + CH_2O(s) \rightarrow CH_3(s) + O(s)$	6.89E + 14	0.65	83.54	$+2.23\theta_{H}$
R 79	$CH_2O(s) \rightarrow CH_2O + Pt(s)$	3.38E + 13	0.81	51.64	
R 80	$CH_2O + Pt(s) \rightarrow CH_2O(s)$	1.47E + 06	0.69	−4.94	
R 81	$Pt(s) + CH_2O(s) \rightarrow HCO(s) + H(s)$	1.32E + 16	0.48	44.59	
R 82	$HCO(s) + H(s) \rightarrow Pt(s) + CH_2O(s)$	4.19E + 14	0.52	56.41	$+2.23\theta_{H}$
R 83	$O(s) + CH_2O(s) \rightarrow HCO(s) + OH(s)$	7.96E + 15	0.47	10.52	$+7.82\theta_{O}$
R 84	$HCO(s) + OH(s) \rightarrow O(s) + CH_2O(s)$	3.60E + 14	0.53	73.38	
R 85	$C_2H_6 + Pt(s) + Pt(s) \rightarrow CH_3(s) + CH_3(s)$	2.71E + 08	0.38	47.97	
R 86	$CH_3(s) + CH_3(s) \rightarrow C_2H_6 + Pt(s) + Pt(s)$	9.76E + 17	0.62	21.33	

conversion to HCO and further decomposition to CO was considered and evaluated via experimental comparisons by Mhadeshwar et al. [26] as well. Although according to the subsequently presented results, the CH_3 radical coupling on the surface to form C_2H_6 has a negligible role on the formation of C_2 products, the consideration of the reversible reaction is important for defining the thermodynamically consistent mechanism and active radical interactions.

The rate constants are provided by a modified Arrhenius equation $k_{fk} = A_k T^{\beta} \exp\left[\frac{-E_{ak}}{RT}\right] \prod_{i=1}^{N_s} \Theta_i^{\mu_{ik}} \exp\left[\frac{\epsilon_{ik}\Theta_i}{RT}\right]$; the adsorption kinetic is represented by sticking coefficients; the surface site density is $\Gamma = 2.72 \times 10^{-9}$ mol/cm^2. A: Sticking coefficient or pre-exponential factor, β: temperature dependency.

To further broaden our understanding of the OCM surface mechanism over platinum, the relative change in the surface coverages between the original CPOX mechanism by Kahle et al. [28] and our newly developed OCM surface mechanism for Pt at the CH_4/O_2 ratio of 1.1 and 50 % N_2 dilution with GHSV of 4.5 × 10^5 h^{-1} is depicted in Fig. 5. The figure describes the species coverages along the channel axis for the most prevalent surface intermediates: O(s), CO(s), H(s), OH(s), and C(s).

In Fig. 5***(a)***, within the first millimeter of the channel, adsorbed oxygen is quickly consumed on the surface. In that area, the presence of O species quickly reduces the amount of H(s) on the surface, which points to an easy oxidation of H(s). In analogy to the total oxidation of methane over noble-metal catalysts, the predominant amount of the total oxidation products CO_2 and H_2O is formed near the catalyst inlet region [48,49]. Hence, the initial excess oxygen makes the front part of the catalyst a total oxidation zone [32]. Once the O(s) concentration is

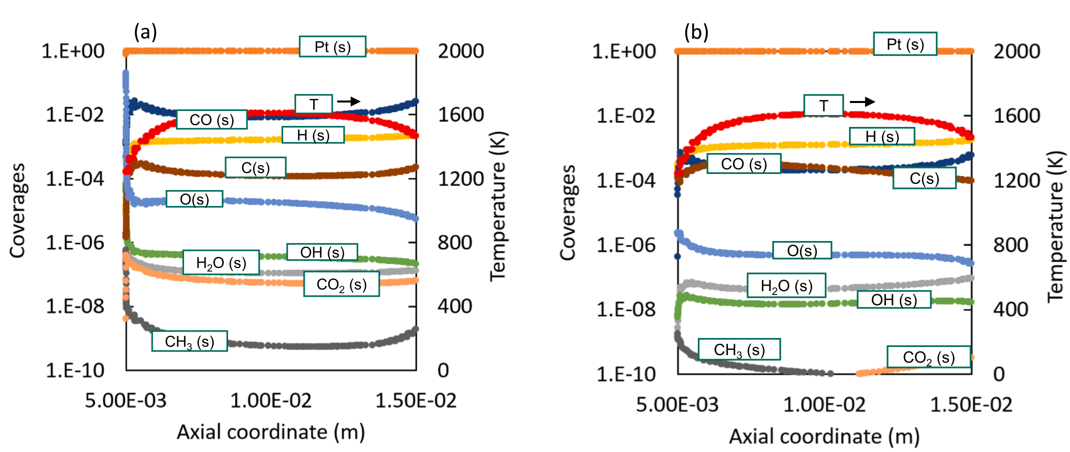

Fig. 5. Numerically predicted surface coverage of adsorbed species as a function of axial position along the catalytic monolith at $CH_4/O_2 = 1.1$, $N_2 = 50$ %, p = 1 bar, GHSV = 4.5 × 10^5 h^{-1}, a) Original mechanism by Kahle et al. [28], b) New OCM surface mechanism. T: red, Pt(s): dark orange, CO(s): navy, H(s): yellow, C(s): brown, O(s): blue, OH(s): green, H_2O(s): light grey, CO_2(s): light orange, CH_3(s): dark grey. (For interpretation of the references to colour in this figure legend, the reader is referred to the web version of this article.)

low enough, larger amounts of the partial oxidation precursors CO(s) and H(s) are generated on the surface, leading to the formation of the partial oxidation products H_2 and CO in the second part of the catalyst.

On the contrary, simulations with the newly developed OCM mechanism comprise the formation and decomposition of oxygenates, which results in an overall lower amount of adsorbed O(s) species, as illustrated in Fig. 5***(b)***. Nevertheless, similar to the simulation conducted with the CPOX mechanism by Kahle et al. [28], adsorbed oxygen is quickly consumed on the surface, followed by CO(s) and H(s) formation on the surface, the new OCM mechanism predicts a decrease in the surface coverages of CO(s), O(s) and OH(s) that is due to the desorption of radicals from the surface to interact in the gas-phase. Notably, the desorption of OH radical species from the Pt surface at temperatures above 1000 K and subsequent their interaction with other reactants in the gas-phase is well established [13,50]. Along with the rise in temperature inside the monolithic catalyst, the relatively high desorption rate of reactive radicals from the surface facilitates the initiation of gas-phase reactions that ultimately convert CH_4 into C_2 species.

In order to ensure an accurate description of OCM over platinum, this newly developed microkinetic surface model was coupled with the ABF gas-phase mechanism [35] (*c.f.* sections 3.4 and 3.5). By performing two-dimensional steady-state simulations in adherence to the methodology described in Fig. 1 and comparing the numerical results with the experimental dataset as presented in the following, we validate the overall reaction network.

4.4. Evaluation of the new surface and gas-phase chemistry reaction network

4.4.1. The impact of different N_2 dilution

N_2 dilution in the feed composition is considered to be an important parameter that influences C_2 yields. For instance, a strong correlation of N_2 dilution, CH_4 conversion, and C_2 yields was observed by Hohn et al. [17] when operating a Pt/Al_2O_3 catalyst at short contact times. In the present study, the experiments at short contact times were conducted with a CH_4/O_2 ratio of 1.1 and a space velocity of 2.9×10^5 h^{-1} while reducing the N_2 dilution in the system from 70 % to 50 % by 5 % per experiment. This reduction in N_2 dilution to 50 % results in a maximum C_2 species selectivity of ca. 10 %. Fig. 6 illustrates that the data on the yield of the product species predicted by the 2D simulations using the newly proposed OCM surface mechanism coupled with the ABF gas-phase mechanism are in good agreement with our experimental data. Also, the simulated temperature curve follows the same trend as the temperature seen in the experiments, namely an increase in temperature with decreasing dilution. The experimental investigations revealed that the conversion of methane was not dependent on the inlet N_2 dilution, which can be attributed to the relatively high temperatures achieved at all operational points. However, as the N_2 dilution was decreased from 70 % to 50 %, the increase in C_2 selectivity corresponds to the increase in temperature downstream of the catalyst. The higher temperature leads to activation of gas-phase chemistry responsible for C_2 formation, discussed in detailed in section 5.4.2. In accordance with our experiments, the simulations point to C_2H_2 as most prominent C_2 product at lower N_2 dilutions.

4.4.2. The impact of different CH_4/O_2 ratios

Considering conditions of 50 % N_2 dilution and a space velocity of 4.5×10^5 h^{-1} over a monolithic 1 wt−% Pt/Al_2O_3 catalyst, experiments were carried out for various CH_4/O_2 ratios ranging from 1.1 to 2.0. Both simulations and experiments show that the conversion of methane was strongly dependent on the inlet CH_4/O_2 ratios, which supports earlier findings [17,32]. In Fig. 7, a rise in CH_4 conversion along with a rise in temperature and C_2 yield was observed at higher inlet CH_4/O_2 ratios. Herein, the proposed kinetic model does not only predict the total C_2 yields very well, but also adequately describes the individual C_2 yields for C_2H_2, C_2H_4 and C_2H_6. The maximum C_2H_2 yield of 10 % was observed at the CH_4/O_2 ratio of 1.1, whereas the maximum C_2H_4 and C_2H_6 yield was obtained at a CH_4/O_2 ratio of 1.4, which tails off when lowering the CH_4/O_2 ratio even further.

4.4.3. The impact of different GHSV

It is consensus that one of the most important factors impacting the C_2 selectivity during OCM is the gas hourly space velocity (GHSV). According to Kooh et al. [51], rising space velocities create a significant temperature difference between the catalyst hotspot and the (furnace) operation temperature, which results in higher C_2 yields. The data visualized in Fig. 8 demonstrate that at a CH_4/O_2 ratio of 1.1, 50 % N_2 dilution, and varying GHSV, the C_2 yield almost plateaus at 10 % yield with 94 % CH_4 conversion for space velocities between 2.9×10^5 h^{-1} and 4.5×10^5 h^{-1}, but drops if the GHSV is further increased. These findings are in line with the observations previously reported by Witt et al. [20] for Rh-based catalysts and point to a direct correlation between GHSV, C_2 yield, and CH_4 conversion. Additionally, a steep decrease in the predicted C_2H_2 yield is considered to be the fact C_2H_2 is formed via C_2H_4 (see. Section 4.5). The drop in the experimentally determined C_2 yield can be attributed to the decreasing CH_4 conversion that is a consequence of reduced contact times over the coated catalyst [52]. Furthermore, diffusion limitations seem to affect the catalytic performance at GHSV above 4.5×10^5 h^{-1} which is not considered in the simulations and are out of the scope of this work. Simultaneously, the temperature observed after the catalyst also declines as the CH_4 conversion decreases. The numerically projected kinetic model (newly developed OCM surface model coupled with the ABF gas-phase mechanism [35]) closely matches the empirically determined product yields as a function of the space velocity and is also capable of predicting the

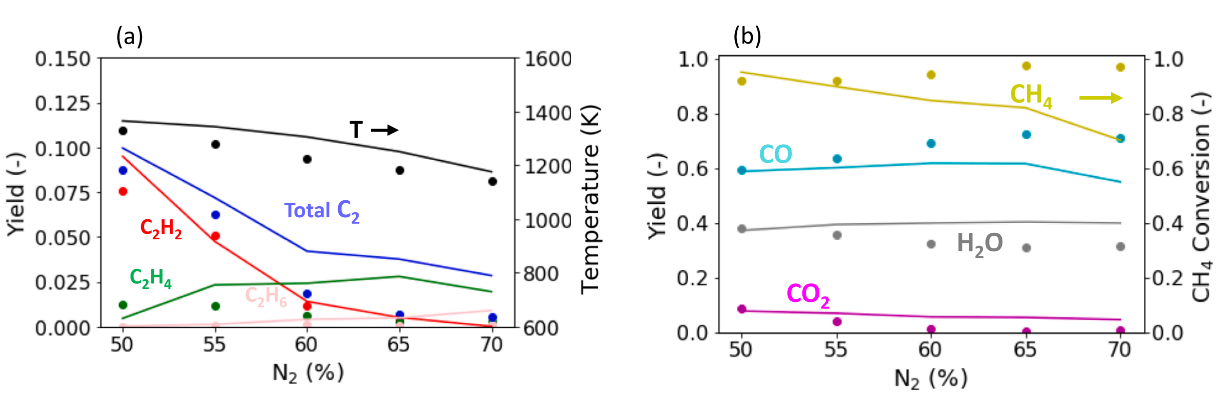

Fig. 6. Comparison of simulated (lines) and measured (points) for the influence of N_2 dilution (CH_4/O_2= 1.1, p = 1 bar, 2.9×10^5 h^{-1}), (a) yield of C_2 species and temperature downstream of monolith (b) CH_4 conversion, yield of CO_x and H_2O species.

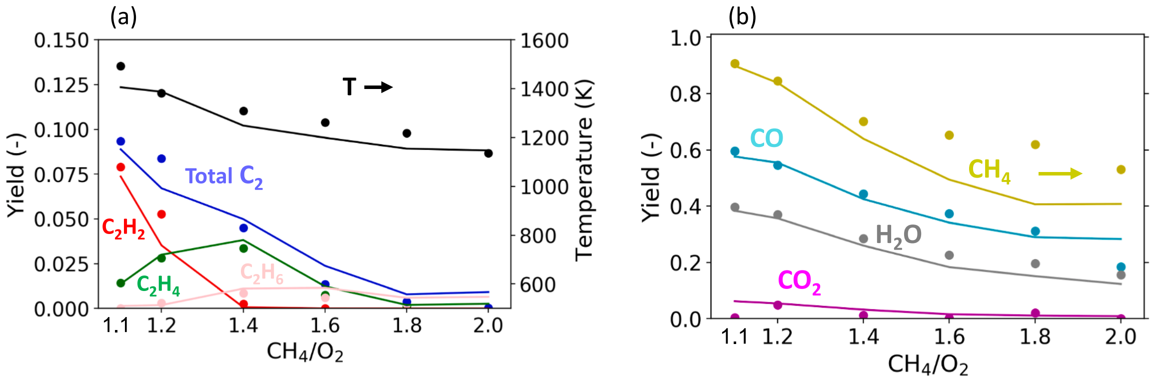

Fig. 7. Comparison of simulated (lines) and measured (points) for the influence of CH_4/O_2 ratio (p = 1 bar, GHSV = 4.5×10^5 h^{-1}, 50 % N_2), (a) yield of C_2 species and temperature downstream of monolith (b) CH_4 conversion, yield of CO_x and H_2O species.

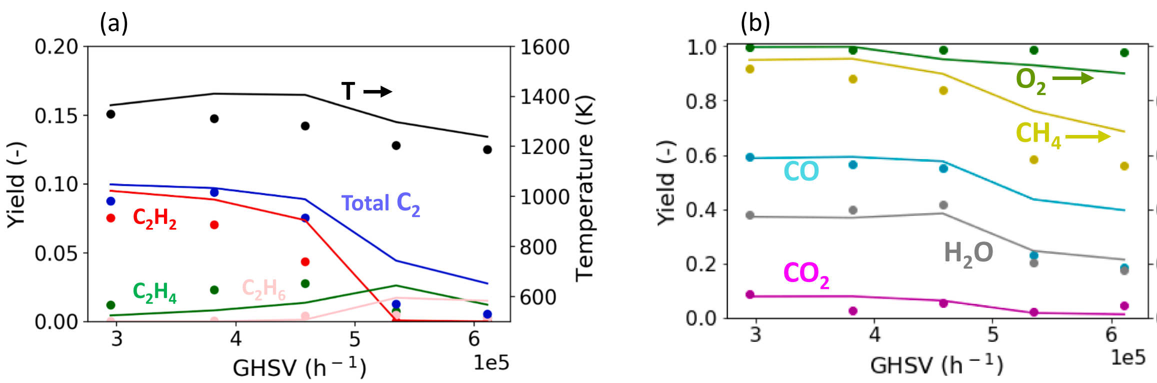

Fig. 8. Comparison of simulated (lines) and measured (points) for the influence of GHSV (CH_4/O_2 = 1.1, p = 1 bar, 50 % N_2), (a) yield of C_2 species and temperature downstream of monolith (b) CH_4 conversion, yield of CO_x and H_2O species.

temperature downstream the catalyst and the overall CH_4 conversion fairly well.

4.5. Mechanistic insights by detailed chemical modeling

4.5.1. The impact of space velocity on surface and gas-phase chemistry

Notably, nearly 70 % of the methane is converted via the heterogenous catalytic reactions at a GHSV of 2.9×10^5 h^{-1}. However, as the GHSV is increased beyond 2.9×10^5 h^{-1}, a decrease in residence time leads to a decline in methane conversion over the surface from 70 % to around 50 % at a space velocity of 6.2×10^5 h^{-1} as depicted in Fig. 9***(a)***, which goes along with a declining oxygen conversion on the surface (Fig. 9***(b))***, i.e. from 75 % at a GHSV of 2.9×10^5 h^{-1} to 60 % at a GHSV of 6.2×10^5 h^{-1}. These trends are responsible for the decline in temperature increase and C_2 yield observed in Fig. 8 upon an increase in the space velocity. On increasing GHSV, the methane conversion attributed to gas phase reactions decreases while the oxygen conversion from gas phase reactions increases. At high GHSV of 6.2×10^5 h^{-1}, maximum temperature of 1300 K is reached. At this temperature, the fact that O_2 is available downstream of the monolith, leads to the formation of oxygenate species via gas phase reactions such as formaldehyde (CH_2O) and ketene (CH_2CO). Similar observation was made by Porras et. al [53]. Additionally, as shown in the reaction flow analysis in 4.5.3 O-assisted pathways are enhanced at lower temperature, in accordance with literature [54].

To comprehend the underlying chemistry and operations further,

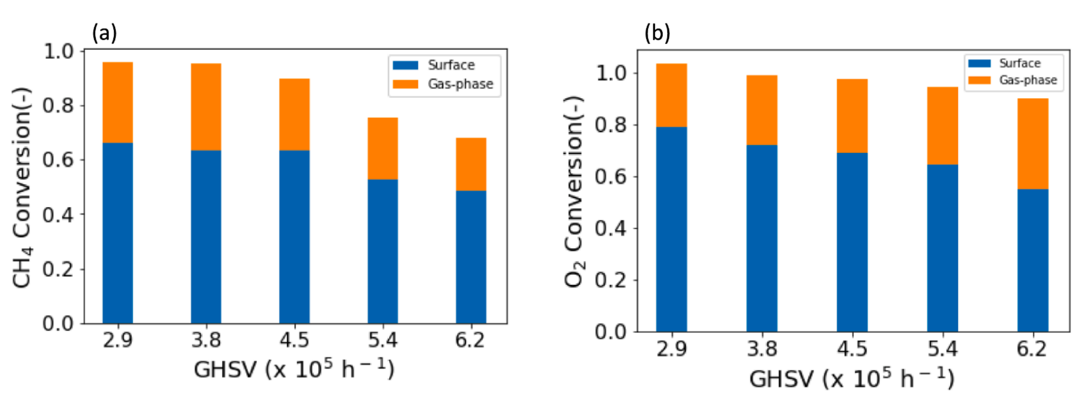

Fig. 9. Numerically predicted contribution of heterogenous and homogenous reaction pathways for the influence of GHSV (CH_4/O_2 = 1.1, p = 1 bar, 50 % N_2), (a) CH_4 conversion (b) O_2 conversion.

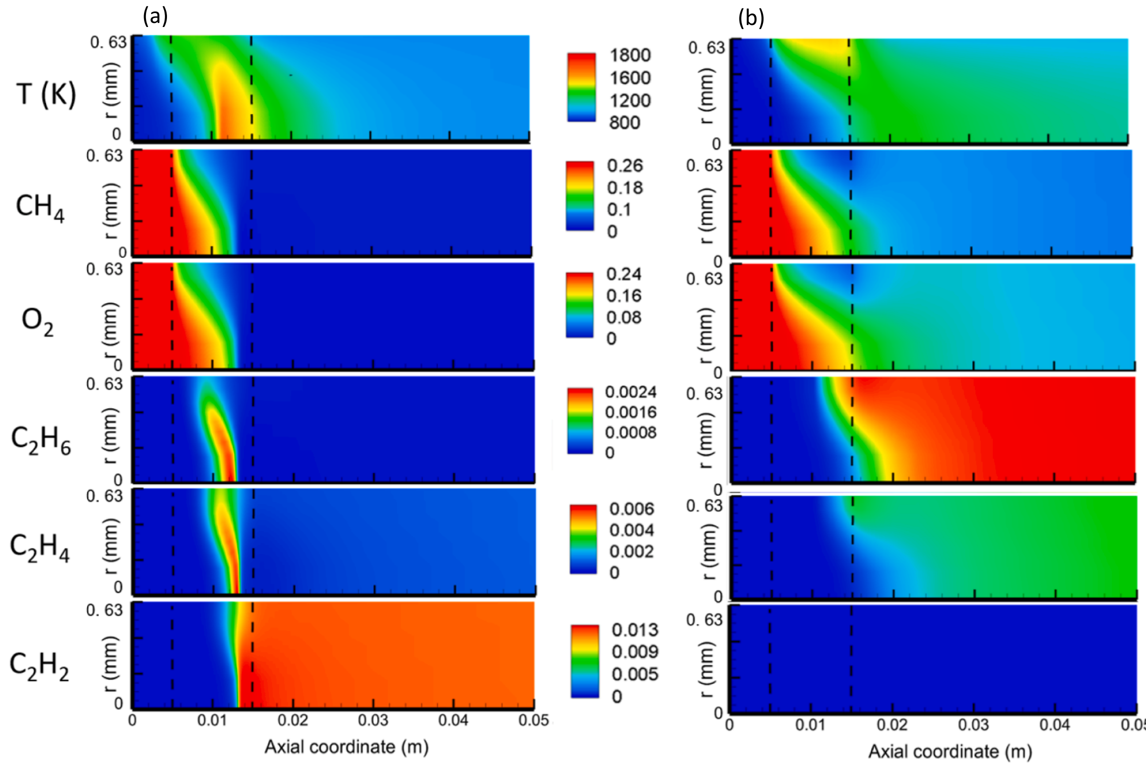

Fig. 10. Numerically simulated two-dimensional profiles of temperature and mole fractions of species over the catalyst and downstream of the catalytic monolith (the length of approximately 0.05 m is shown in the figure) at $CH_4/O_2 = 1.1$, $N_2 = 50$ %, p = 1 bar) at a GHSV of a) 2.9×10^5 h^{-1} and b) 6.2×10^5 h^{-1}.

Fig. 10 depicts the simulated concentration flow fields and gas-phase temperature contours in two dimensions for a feed with a CH_4/O_2 ratio of 1.1 and 50 % N_2 dilution at for the minimum (2.9×10^5 h^{-1}) and maximum (6.2×10^5 h^{-1}) GHSV that was tested experimentally. In Fig. 10***(a)***, at a space velocity of 2.9×10^5 h^{-1}, the CH_4 and O_2 contours show that there are significant external gradients at the channel's entry. Along the length of the channel, a rise in temperature to above 1800 K along with depletion of oxygen is observed. The C_2H_6 contour evolution is typical for a species that is quickly created in the gas-phase over the catalyst and subsequently undergoes dehydrogenation to C_2H_4 and C_2H_2 along the channel length. Furthermore, C_2 formation begins before oxygen is completely consumed over the catalyst sample and continues until almost all the available methane is converted. An increase of the GHSV to 6.2×10^5 h^{-1}, results in a lower residence time, which thereafter leads to a lower conversion of reactants, a relatively lower maximum temperature of around 1300 K over the catalyst, and ultimately to lower C_2 formation (Fig. 10***(b)***). Not all of the oxygen is consumed over the catalyst. Incomplete oxygen conversion over the catalyst surface was also observed in the high temperature catalysis experiments over Pt in literature [34,55]. Additionally, 2D axial simulations depict that the oxygen consumption continues in the region downstream of the catalyst where the temperature is still sufficiently high to allow for gas-phase reactions. In contrast to lower space velocities, predominantly C_2H_6 and C_2H_4 are formed, whereas the evolving C_2H_2 concentrations are negligible. As discussed in the following section, the C_2 product distribution is strongly governed by the reaction temperature.

4.5.2. The C_2 formation temperature

The data discussed so far and the 2D simulations in the previous section in particular underscore that the C_2 yield is strongly influenced by the temperature rise inside the catalytic reactor. The increasing space velocity results in a decreasing residence time over the catalyst sample and consequently lower temperatures are reached inside the reactor. Fig. 8 demonstrates that the C_2 yields plateaus at space velocities between 2.9 and 4.5×10^5 h^{-1}. A further rise in space velocity causes a drop in the C_2H_2 yield and gives rise to the C_2H_4 yield instead. In order to uncover the underlying phenomena, Fig. 11 depicts the C_2 yields as a function of temperature over the catalyst sample for a GHSV of 2.9×10^5 h^{-1}, 4.5×10^5 h^{-1} and 6.2×10^5 h^{-1} as obtained by numerical simulations using our newly developed OCM surface reaction mechanism coupled with the ABF gas-phase mechanism. The higher temperature of above 1800 K reached for a GHSV of 2.9×10^5 h^{-1} led to a C_2H_2 yield of 9 % and a C_2H_4 yield of 1 %, whereas the model predicts a C_2H_2 yield of about 6 % and a C_2H_4 yield of 3 % at 1700 K for a GHSV of 4.5×10^5 h^{-1}. In case of 6.2×10^5 h^{-1}, the temperature rises to 1300 K, leading to C_2H_6 and C_2H_4 formation 2 % total C_2 yield. From a mechanistic point of view, high temperatures benefit the dehydrogenation reaction pathways in our kinetic model, which does not only influence the total C_2 yields but also the C_2 product distribution. According to our model, a minimum temperature of 1200 K is required to allow for C_2H_6 and C_2H_4 formation, whereas C_2H_2 formation starts at approximately 1400 K. Notably, almost 1700 K are required for C_2H_2 becoming the predominant product among the C_2 species.

4.5.3. Reaction flow analysis

Reaction flow analysis was performed considering individually the proposed surface mechanism and the gas-phase mechanism due to computational limitations. Reaction flow analysis of the catalytic conversion of methane is conducted at initial temperature of 773 K with adiabatic conditions at $CH_4/O_2 = 1.1$, $N_2 = 50$ %, p = 1 bar, GHSV = 4.5 $\times 10^5$ h^{-1}. However, during the gas-phase reaction flow analysis studies, the maximum temperature reached inside the reactor for the particular GHSV, GHSV = 2.9×10^5 h^{-1} ($T_{max} = 1800$ K) and GHSV = 6.2×10^5 h^{-1} ($T_{max} = 1300$ K), was considered for isothermal batch reaction flow analysis studies.

Heterogenous Reactions

In order to gain further mechanistic insights, Fig. 12 depicts a

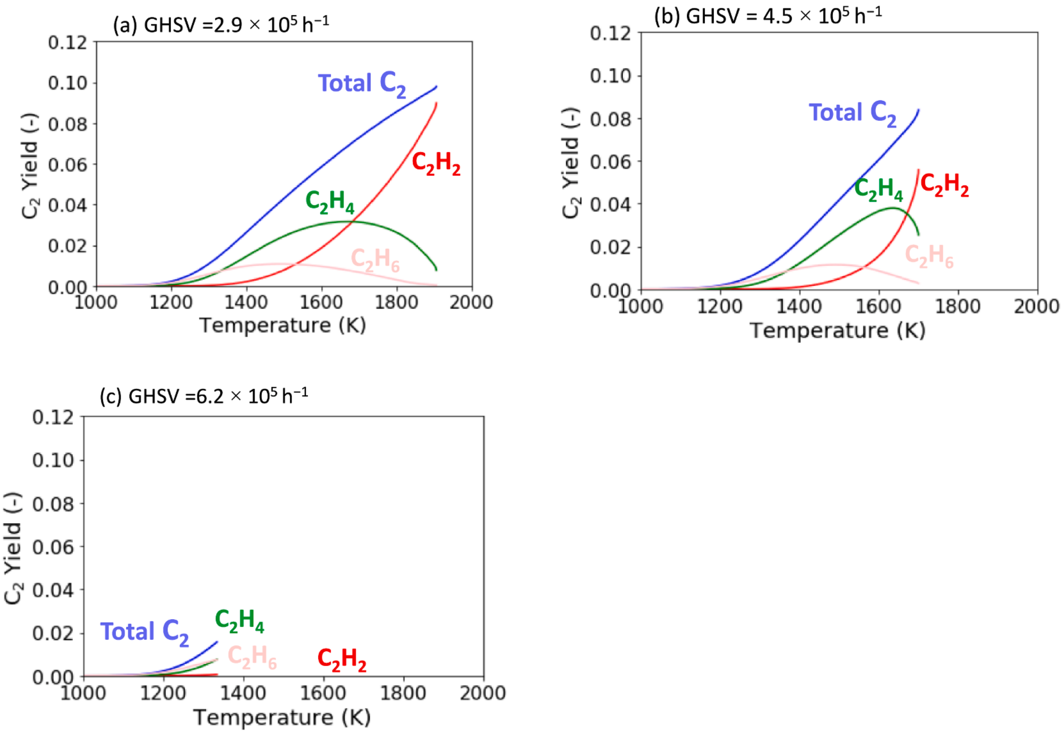

Fig. 11. Numerically simulated C_2 yield as a function of temperature at three different GHSVs ($CH_4/O_2 = 1.1$, $N_2 = 50$ %, $p = 1$ bar), a) GHSV = 2.9×10^5 h^{-1}b) GHSV = 4.5×10^5 h^{-1}c) GHSV = 6.2×10^5 h^{-1}.

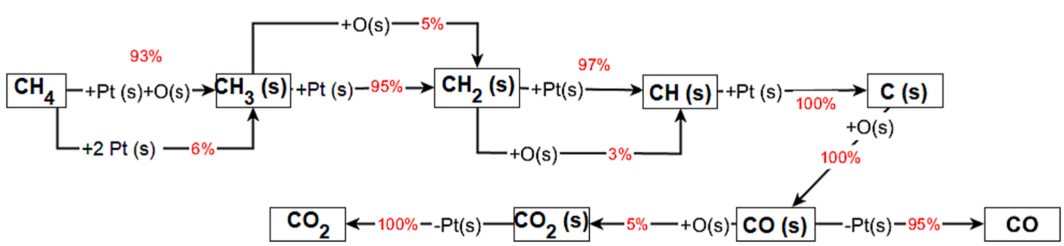

Fig. 12. Reaction flow analysis of the catalytic conversion of methane at initial temperature of 773 K with adiabatic conditions at the $CH_4/O_2 = 1.1$, $N_2 = 50$ %, p = 1 bar, GHSV = 4.5×10^5 $h^{-1.}$ Only major pathways are included.

reaction flow analysis (RFA) of C-species that was conducted for our newly developed OCM mechanism at an initial temperature of 773 K with adiabatic conditions at the CH_4/O_2 ratio of 1.1, 50 % N_2 dilution, and at the intermediate GHSV of 4.5×10^5 h^{-1} where both adequate high temperature and C_2 yields are visualized in the previous section. As an initial step in the RFA, CH_4 undergoes oxidative dehydrogenation on the surface to form CH_3(s) radicals that are adsorbed on the surface and get further transformed to CH_2(s) and CH(s). This CH_x dehydrogenation on the Pt surface is primarily a thermal process and ultimately results in the production of C(s). C(s) formation is the dominant decomposition path. Subsequently, C(s) is oxidized to CO(s), which eventually desorbs. The oxidative thermal decomposition of CH_4 over Pt leads high temperatures, where most of the CO(s) desorbs, resulting in surface vacancies. A further reaction of C(s) with adsorbed oxygen (O(s)) leads to CO(s) formation. While the predominant share of CO(s) species desorbs due to the pronounced heat evolution, a minor amount of 5 % reacts with O(s) to form CO_2(s) that ultimately desorbs as well. Furthermore, H (s) interacts with another H(s) and O(s) to produce H_2 and H_2O, respectively.

In summary, almost all the methane on the surface is consumed to form CO and CO_2. Despite the incorporation of a CH_3 radical coupling pathway in the surface mechanism, the contribution of heterogenous surface reactions to the formation of C_2 species is negligible under the conditions considered. Nevertheless, the exothermicity of the total and partial oxidation reactions results in a pronounced heat evolution, which is considered a key parameter for the homogeneous reaction network that is discussed next.

Homogenous Reactions

The gas-phase mechanism for methane consumption evolves gradually once the temperature inside the reactor exceeds 1200 K and becomes significant in addition to the heterogeneous surface reactions. The major pathways involved in the gas-phase consumption of methane do not only comprise oxidative routes but also pyrolytic pathways. Notably, the methyl (CH_3) radical formation from CH_4 takes place via three major routes: Either via an H radical (R1), or an OH radical (R2), or an O radical (R3) attack on CH_4.

$$CH_4 + H^{\bullet} \rightleftharpoons CH_3^{\bullet} + H_2 \tag{R1}$$

$$CH_4 + OH^{\bullet} \rightleftharpoons CH_3^{\bullet} + H_2O \tag{R2}$$

$$CH_4 + O^{\bullet} \rightleftharpoons CH_3^{\bullet} + OH^{\bullet} \tag{R3}$$

Further reactions of these CH_3 radicals ultimately lead to C_2 species formation. However, as discussed above, the inlet feed conditions greatly impact the C_2 product distribution and yield, resulting in higher

C_2 yields at lower space velocity and higher residence time. To understand the underlying chemistry in the gas-phase, a detailed RFA was conducted for the ABF mechanism, hereby choosing two operating conditions that correspond to the two-dimensional species profiles depicted in Fig. 10, one at a higher temperature of 1800 K achieved at a GHSV of $2.9 \times 10^5\ h^{-1}$, where oxygen consumption is complete over the catalyst sample, and another at a lower temperature of 1300 K achieved at a GHSV of $6.2 \times 10^5\ h^{-1}$, where oxygen consumption is incomplete at the catalyst sample.

As already discussed in the context of Fig. 10***(a)***, the optimal residence time enables consumption of methane and oxygen along the Pt catalytic monolith at high temperature around 1800 K when choosing a space velocity of GHSV $2.9 \times 10^5\ h^{-1}$. Under these conditions, heterogenous catalytic reactions contribute to almost 70 % to the methane consumption, exclusively leading to CO and CO_2 formation as elucidated in Fig. 9. In addition, a further conversion of methane takes place in the gas-phase as depicted in the Fig. 13.

With 67 % of the overall consumption of CH_4 in the gas-phase, the pyrolytic pathway (R1) dominates at higher temperatures, which can be traced back to the strong depletion of oxygen. The methyl (CH_3) radical formation from methane via the reaction with OH (R2) and O (R3) radicals accounts for 21 % and 7 % respectively. In a second step, the CH_3 radicals formed in the gas-phase combine to form C_2H_6 (R4) or a C_2H_5 (R5) radical, which further undergoes thermal dehydrogenation to form C_2H_4 (R6).

$$CH_3^\bullet + CH_3^\bullet \rightleftharpoons C_2H_6 \tag{R4}$$

$$CH_3^\bullet + CH_3^\bullet \rightleftharpoons C_2H_5^\bullet + H^\bullet \tag{R5}$$

$$C_2H_5^\bullet + M \rightleftharpoons C_2H_4 + H^\bullet \tag{R6}$$

Prior to the sequential dehydrogenation of C_2H_4 to C_2H_2, the reaction flow analysis suggests ethylidyne (C_2H_3 radical) acting as an intermediator. The thermal decomposition of C_2H_4 to ethylidyne proceeds mainly via the reaction R(7), which contributes up to 77 %. Although this makes ethylidyne an important intermediate radical in the reaction pathway, almost all of it is rapidly converted into C_2H_2 via reaction R(8).

$$C_2H_4 + H \rightleftharpoons C_2H_3^\bullet + H_2 \tag{R7}$$

$$C_2H_3^\bullet + M + H^\bullet \rightleftharpoons C_2H_2 + H_2 \tag{R8}$$

Beyond the desired target product C_2H_2, the presence of oxygen radicals can lead to a further oxidation of C_2H_2, resulting in the formation of HCCO and CH_2CO species. Although the predominant share of the HCCO radicals contribute to CO formation, a part of these species is consumed to regenerate C_2H_4 and CH_3 radicals, respectively.

When a substantially higher GHSV of $6.2 \times 10^5\ h^{-1}$ is chosen instead, the extremely low residence time of reaction species over the catalyst leads to an only poor interaction of feed gases with the surface, which causes a relatively lower temperature rise to 1300 K shown in Fig. 10***(b)***. Therefore, there is a lower conversion of CH_4 and O_2 over the surface. With the onset of gas-phase chemistry above 1200 K, CH_3 radicals are continuously generated in the gas-phase by the both oxygen-assisted and pyrolytic routes. The reaction flow analysis conducted for 1300 K that is summarized in Fig. 14 suggests that due to the high amount of oxygen species in the gas-phase, the reaction of CH_4 with OH radical dominates as the main source (64 %) of CH_3 radicals, in clear contrast to the dominating pyrolytic path at temperatures as high as 1800 K. Furthermore, 25 % of the generated CH_3 radicals undergoes oxidation to form CH_2O, which transform into HCO radicals upon molecular oxidation, thereby ultimately contributing to CO evolution.

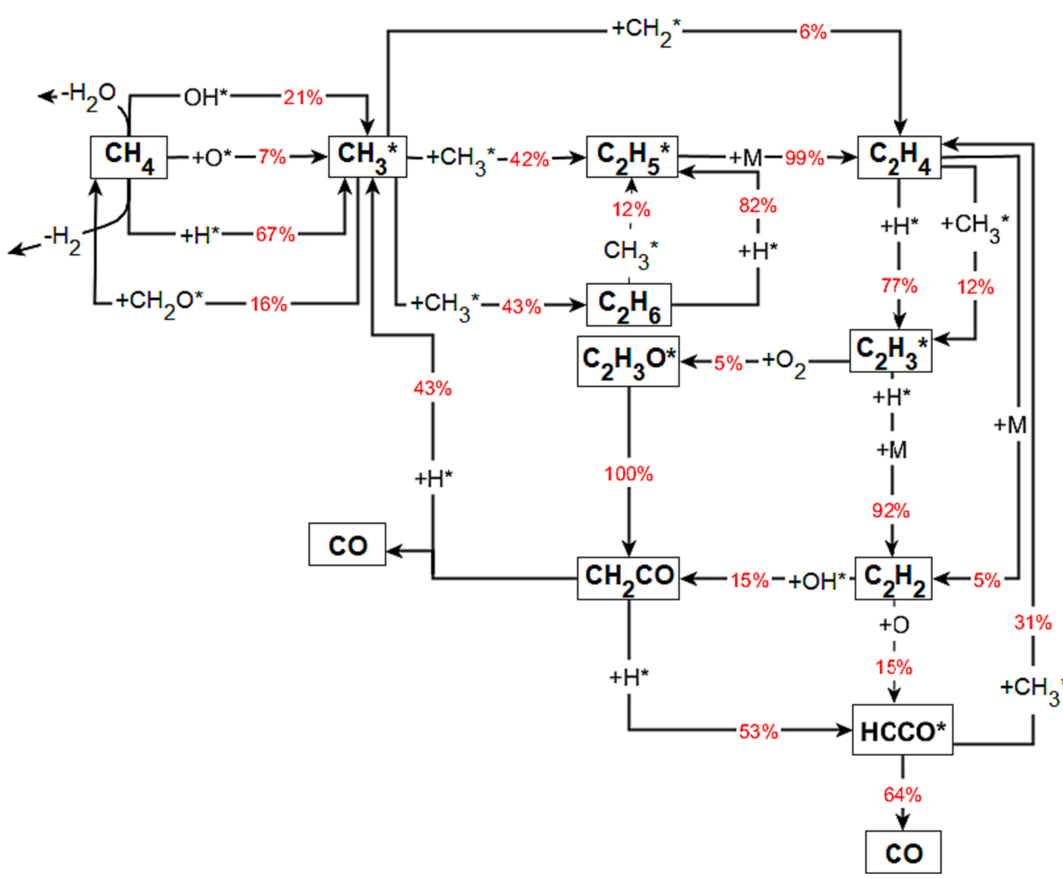

Fig. 13. Reaction flow analysis of the homogenous conversion of methane using ABF mechanism [35] in a batch reactor at a temperature of 1800 K at the inlet conditions of $CH_4/O_2 = 1.1$, $N_2 = 50$ %, p = 1 bar. Only major pathways affecting C_2 formation are included.

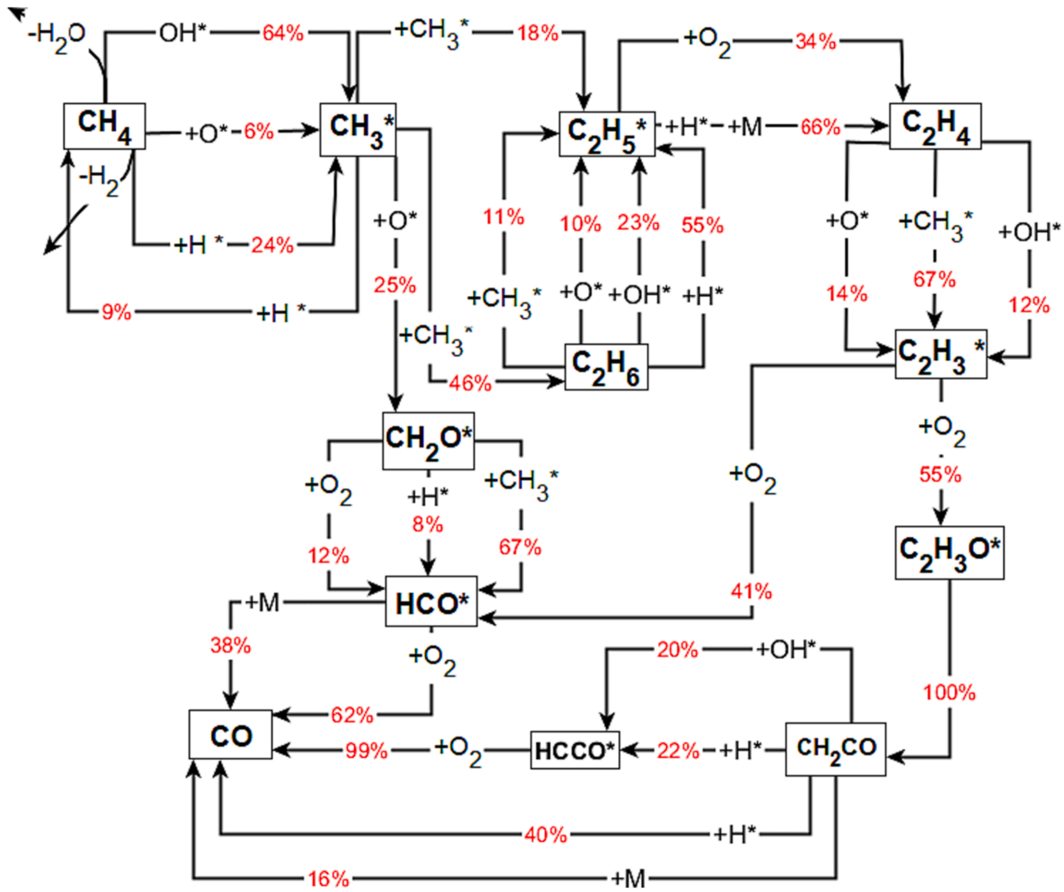

Fig. 14. Reaction flow analysis of the homogenous conversion of methane with ABF mechanism [35] in a batch reactor at a temperature of 1300 K at the $CH_4/O_2 = 1.1$, $N_2 = 50$ %, p = 1 bar. Only major pathways affecting C_2 formation are included.

In addition, the RFA suggests a fast dehydrogenation mechanism enabling the C_2H_4 formation through C_2H_6 via both a thermal and an oxidative route. The subsequent decrease in C_2H_4 is mainly caused by a further transformation to ethylidyne (C_2H_3 radical), once again via both an oxidative (reaction with O or OH radicals) and a pyrolytic route (reaction with a CH_3 radical). Ethylidyne, thereafter, undergoes oxidation and contributes to the formation of intermediatory radicals like HCO (R9), C_2H_3O (R10) and HCCO (R12). C_2H_3O radical further transforms to CH_2CO via R11.

$$C_2H_3^{\bullet} + O_2 \rightleftharpoons HCO^{\bullet} + CH_2CO \quad \text{(R9)}$$

$$C_2H_3^{\bullet} + O_2 \rightleftharpoons C_2H_3O^{\bullet} + O^{\bullet} \quad \text{(R10)}$$

$$C_2H_3O^{\bullet} \rightleftharpoons CH_2CO + H^{\bullet} \quad \text{(R11)}$$

$$CH_2CO + H^{\bullet} \rightleftharpoons HCCO^{\bullet} + H_2 \quad \text{(R12)}$$

Ultimately, these active O-containing radicals facilitate the generation of CO via CH_2CO (R13), HCCO (R14), and HCO (R15):

$$CH_2CO + H^{\bullet} \rightleftharpoons CO + CH_3^{\bullet} \quad \text{(R13)}$$

$$HCCO^{\bullet} + O_2 \rightleftharpoons 2CO + OH^{\bullet} \quad \text{(R14)}$$

$$HCO^{\bullet} + O_2 \rightleftharpoons CO + HO_2^{\bullet} \quad \text{(R15)}$$

5. Conclusions

The conversion of methane over a Pt-based catalyst operated at short contact times has been studied experimentally and computationally. A novel mechanism is proposed, which consists of the literature surface mechanism for dry reforming over Pt [28] with extensions to account for more reactions and a reaction mechanism for homogeneous reactions from literature (ABF) [35]. The new OCM surface model development involved the expansion of an existing dry reforming mechanism by inclusion of new species like HCO, CH_2O and their interactive reactions on the surface. In particular, 14 new reversible reactions that account for dehydrogenation were incorporated and thereafter, the thermodynamic consistent of the new model was maintained.

The experimental investigation over Pt/Al_2O_3 coated monoliths included variation in input parameters like N_2 dilution, CH_4/O_2 ratio and space velocity, which have a strong correlation with the output C_2 yield. Reducing N_2 dilution and CH_4/O_2 ratio and raising GHSV leads to high C_2 yields. However, experimentally the maximum C_2 yield of 10 % was observed over the 1 wt−% Pt/Al_2O_3 monolithic catalyst at a CH_4/O_2 ratio of 1.1 and 50 % N_2 dilution with a GHSV of 4.5×10^5 h^{-1}.

2D transient simulation studies demonstrated that an adiabatic axial heat transfer along the reactor length led to the rise in temperature before the coated catalyst and played an important role in temperature profile prediction. Thus, this information can be used for designing optimized converters in the future. Notably, the progress in additive manufacturing may facilitate the design and production of advanced geometries, preferentially governed by model-based insights.

The coupling of the new OCM surface model with gas-phase chemistry resulted in a good agreement between computational predictions and experimental results. It was discovered that under the current conditions, the interaction of the feed gases CH_4 and O_2 over the Pt catalyst lead to adiabatic rise in temperature inside the catalyst. The main pathways on the surface lead to total oxidation and partial oxidation of methane that result in CO_2 and CO evolution are the main pathways on the Pt surface. Despite the consideration of the C_2H_6

formation reaction over the Pt surface, the reaction flow analysis does not suggest a significant formation of C_2 on the surface.

Instead, the C_2 yield is strongly influenced by the rise in temperature inside the catalytic reactor and a minimum temperature of 1200 K was required for the activation of C_2 formation. CH_4 undergoes both pyrolytic and oxidative dehydrogenation in the gas-phase to generate CH_3 radicals, which further combine to form C_2 species. Thereby, at high temperatures, both oxidative and pyrolytic routes play a role in achieving the high C_2 yields. However, the very high availability of oxygen in the gas-phase at lower temperatures resulting from a lower catalytic activity on the surface, leads to a pronounced oxidation of CH_3 radicals and the C_2 species formed in the gas-phase, hereby reducing the product yields.

This approach serves as a cornerstone for autothermal C_2 formation studies at high temperature for which both surface and gas-phase reactions are crucial for conversion of methane at atmospheric pressure. The detailed model that is offered can help with the design and improvement of catalytic short contact time monolithic reactors that are operated at high temperatures. The study provides the best reactor conditions for the operation of the monolithic catalytic reactors in a laboratory or commercial scale, along with mechanistic explanations for why specific temperature, space velocity, and reactive gas composition regimes pose a significant role for catalyst performance for C_2 formation. In future studies, catalyst formulation can be modified to look into the effect of Pt concentration and support material in defining the high C_2 yields.

CRediT authorship contribution statement

Jaspreet Chawla: Data curation, Formal analysis, Investigation, Writing – original draft. **Sven Schardt:** Investigation. **Patrick Lott:** Investigation, Supervision, Writing – review & editing. **Sofia Angeli:** Funding acquisition, Investigation, Supervision, Writing – review & editing. **Steffen Tischer:** Conceptualization, Investigation, Software, Supervision, Validation, Writing – review & editing. **Lubow Maier:** Conceptualization, Methodology, Supervision. **Olaf Deutschmann:** Conceptualization, Funding acquisition, Project administration, Software, Supervision, Writing – review & editing.

Declaration of competing interest

The authors declare that they have no known competing financial interests or personal relationships that could have appeared to influence the work reported in this paper.

Data availability

Data will be made available on request.

Acknowledgments

The authors gratefully acknowledge the 'Helmholtz-BASF Research Collaboration Program' for the financial support (reference KW BASF 5). We acknowledge the very useful support by omegadot software & consulting GmbH for providing the software tool DETCHEM. S.A. Schunk (hte GmbH) is acknowledged for fruitful discussions.

References

[1] J.H. Lunsford, The catalytic oxidative coupling of methane, Angew. Chemie Int. Ed. English. 34 (1995) 970–980, https://doi.org/10.1002/anie.199509701.

[2] R. Horn, R. Schlögl, Methane activation by heterogeneous catalysis, Catal. Letters. 145 (2015) 23–39, https://doi.org/10.1007/s10562-014-1417-z.

[3] B. Wang, S. Albarracín-Suazo, Y. Pagán-Torres, E. Nikolla, Advances in methane conversion processes, Catal. Today. 285 (2017) 147–158, https://doi.org/10.1016/j.cattod.2017.01.023.

[4] W. Taifan, J. Baltrusaitis, CH_4 conversion to value added products: potential, limitations and extensions of a single step heterogeneous catalysis, Appl. Catal. B Environ. 198 (2016) 525–547, https://doi.org/10.1016/j.apcatb.2016.05.081.

[5] D. Bajec, A. Kostyniuk, A. Pohar, B. Likozar, Micro-kinetics of non-oxidative methane coupling to ethylene over Pt/CeO_2 catalyst, Chem. Eng. J. 396 (2020) 125182, https://doi.org/10.1016/j.cej.2020.125182.

[6] M. Wolf, O. Deutschmann, F. Behrendt, J. Warnatz, Kinetic model of an oxygen-free methane conversion on a platinum catalyst, Catal. Letters. 61 (1999) 15–25, https://doi.org/10.1023/a:1019039931310.

[7] A.M. Arinaga, M.C. Ziegelski, T.J. Marks, Alternative oxidants for the catalytic oxidative coupling of methane, Angew. Chemie - Int. Ed. 60 (2021) 10502–10515, https://doi.org/10.1002/anie.202012862.

[8] A. Cruellas, T. Melchiori, F. Gallucci, M. van Sint Annaland, Advanced reactor concepts for oxidative coupling of methane, Catal. Rev. - Sci. Eng. 59 (2017) 234–294, https://doi.org/10.1080/01614940.2017.1348085.

[9] C. Karakaya, R.J. Kee, Progress in the direct catalytic conversion of methane to fuels and chemicals, Prog. Energy Combust. Sci. 55 (2016) 60–97, https://doi.org/10.1016/j.pecs.2016.04.003.

[10] B.C. Michael, D.N. Nare, L.D. Schmidt, Catalytic partial oxidation of ethane to ethylene and syngas over Rh and Pt coated monoliths: Spatial profiles of temperature and composition, Chem. Eng. Sci. 65 (2010) 3893–3902, https://doi.org/10.1016/j.ces.2010.03.033.

[11] D.A. Hickman, L.D. Schmidt, Synthesis gas formation by direct oxidation of methane over Pt monoliths, J. Catal. 138 (1992) 267–282, https://doi.org/10.1016/0021-9517(92)90022-A.

[12] D.A. Hickman, L.D. Schmidt, The role of boundary layer mass transfer in partial oxidation selectivity, J. Catal. 136 (1992) 300–308, https://doi.org/10.1016/0021-9517(92)90063-N.

[13] D.A. Hickman, L.D. Schmidt, Steps in CH4 oxidation on Pt and Rh surfaces: High-temperature reactor simulations, AIChE J. 39 (1993) 1164–1177, https://doi.org/10.1002/aic.690390708.

[14] D.A. Hickman, L.D. Schmidt, Production of syngas by direct catalytic oxidation of methane, Science 259 (1993) 343–346, https://doi.org/10.1126/science.259.5093.343.

[15] M. Huff, L.D. Schmidt, Ethylene formation by oxidative dehydrogenation of ethane over monoliths at very short contact times, J. Phys. Chem. 97 (1993) 11815–11822, https://doi.org/10.1021/j100147a040.

[16] O. Deutschmann, L.D. Schmidt, Modeling the partial oxidation of methane in a short-contact-time reactor, AIChE J. 44 (1998) 2465–2477, https://doi.org/10.1002/aic.690441114.

[17] K.L. Hohn, P.M. Witt, M.B. Davis, L.D. Schmidt, Methane coupling to acetylene over Pt-coated monoliths at millisecond contact times, Catal. Letters. 54 (1998) 113–118, https://doi.org/10.1023/A:1019092308769.

[18] A. Beretta, G. Groppi, A. Carrera, A. Donazzi, Analysis of the Impact of Gas-Phase Chemistry in Adiabatic CPO Reactors by Axially Resolved Measurements (2017), https://doi.org/10.1016/bs.ache.2017.09.001.

[19] O. Korup, R. Schlögl, R. Horn, Carbon formation in catalytic partial oxidation of methane on platinum: model studies on a polycrystalline Pt foil, Catal. Today. 181 (2012) 177–183, https://doi.org/10.1016/j.cattod.2011.04.051.

[20] P.M. Witt, L.D. Schmidt, Effect of flow rate on the partial oxidation of methane and ethane, J. Catal. 163 (1996) 465–475, https://doi.org/10.1006/jcat.1996.0348.

[21] D.K. Zerkle, M.D. Allendorf, M. Wolf, O. Deutschmann, Understanding homogeneous and heterogeneous contributions to the platinum-catalyzed partial oxidation of ethane in a short-contact-time reactor, J. Catal. 196 (2000) 18–39, https://doi.org/10.1006/jcat.2000.3009.

[22] J. Koop, O. Deutschmann, Detailed surface reaction mechanism for Pt-catalyzed abatement of automotive exhaust gases, Appl. Catal. B Environ. 91 (2009) 47–58, https://doi.org/10.1016/j.apcatb.2009.05.006.

[23] O. Korup, C.F. Goldsmith, G. Weinberg, M. Geske, T. Kandemir, R. Schlögl, R. Horn, Catalytic partial oxidation of methane on platinum investigated by spatial reactor profiles, spatially resolved spectroscopy, and microkinetic modeling, J. Catal. 297 (2013) 1–16, https://doi.org/10.1016/j.jcat.2012.08.022.

[24] R.S. Vincent, R.P. Lindstedt, N.A. Malik, I.A.B. Reid, B.E. Messenger, The chemistry of ethane dehydrogenation over a supported platinum catalyst, J. Catal. 260 (2008) 37–64, https://doi.org/10.1016/j.jcat.2008.08.014.

[25] P. Aghalayam, Y.K. Park, N. Fernandes, V. Papavassiliou, A.B. Mhadeshwar, D. G. Vlachos, A C1 mechanism for methane oxidation on platinum, J. Catal. (2003), https://doi.org/10.1016/S0021-9517(02)00045-3.

[26] A.B. Mhadeshwar, D.G. Vlachos, A catalytic reaction mechanism for methane partial oxidation at short contact times, reforming, and combustion, and for oxygenate decomposition and oxidation on platinum, Ind. Eng. Chem. Res. 46 (2007) 5310–5324, https://doi.org/10.1021/ie070322c.

[27] R. Quiceno, J. Pérez-Ramírez, J. Warnatz, O. Deutschmann, Modeling the high-temperature catalytic partial oxidation of methane over platinum gauze: detailed gas-phase and surface chemistries coupled with 3D flow field simulations, Appl. Catal. A Gen. 303 (2006) 166–176, https://doi.org/10.1016/j.apcata.2006.01.041.

[28] L.C.S. Kahle, T. Roussière, L. Maier, K. Herrera Delgado, G. Wasserschaff, S. A. Schunk, O. Deutschmann, Methane dry reforming at high temperature and elevated pressure: impact of gas-phase reactions, Ind. Eng. Chem. Res. 52 (2013) 11920–11930, https://doi.org/10.1021/ie401048w.

[29] R. Horn, K.A. Williams, N.J. Degenstein, A. Bitsch-Larsen, D. Dalle Nogare, S. A. Tupy, L.D. Schmidt, Methane catalytic partial oxidation on autothermal Rh and Pt foam catalysts : oxidation and reforming zones, transport effects, and approach to thermodynamic equilibrium, J. Catal. 249 (2007) 380–393, https://doi.org/10.1016/j.jcat.2007.05.011.

[30] D. Dalle Nogare, N.J. Degenstein, R. Horn, P. Canu, L.D. Schmidt, Modeling spatially resolved profiles of methane partial oxidation on a Rh foam catalyst with detailed chemistry, J. Catal. 258 (2008) 131–142, https://doi.org/10.1016/j.jcat.2008.06.006.
[31] R. Horn, N.J. Degenstein, K.A. Williams, L.D. Schmidt, Spatial and temporal profiles in millisecond partial oxidation processes, Catal. Letters. 110 (2006) 169–178, https://doi.org/10.1007/s10562-006-0117-8.
[32] J. Chawla, S. Schardt, S. Angeli, P. Lott, S. Tischer, L. Maier, O. Deutschmann, Oxidative coupling of methane over Pt/Al2O3 at high temperature: multiscale modeling of the catalytic monolith, Catalysts. 12 (2022) 189, https://doi.org/10.3390/catal12020189.
[33] A. Beretta, E. Ranzi, P. Forzatti, Oxidative dehydrogenation of light paraffins in novel short contact time reactors. experimental and theoretical investigation, Chem. Eng. Sci. 56 (2001) 779–787, https://doi.org/10.1016/S0009-2509(00)00289-X.
[34] M. Geske, K. Pelzer, R. Horn, F.C. Jentoft, R. Schlögl, In-situ investigation of gas phase radical chemistry in the catalytic partial oxidation of methane on Pt, Catal. Today. 142 (2009) 61–69, https://doi.org/10.1016/j.cattod.2009.01.005.
[35] J. Appel, H. Bockhorn, M. Frenklach, Kinetic modeling of soot formation with detailed chemistry and physics: Laminar premixed flames of C_2 hydrocarbons, Combust. Flame. 121 (2000) 122–136, https://doi.org/10.1016/S0010-2180(99)00135-2.
[36] K.A. Karinshak, P. Lott, M.P. Harold, O. Deutschmann, In situ activation of bimetallic Pd−Pt methane oxidation catalysts, ChemCatChem. 12 (2020) 3712–3720, https://doi.org/10.1002/cctc.202000603.
[37] A. Bruix, J.T. Margraf, M. Andersen, K. Reuter, First-principles-based multiscale modelling of heterogeneous catalysis, Nat. Catal. 2 (2019) 659–670, https://doi.org/10.1038/s41929-019-0298-3.
[38] P. Lott, O. Deutschmann, Heterogeneous chemical reactions — A cornerstone in emission reduction of local pollutants and greenhouse gases, Proc. Combust. Inst. 000 (2022) 1–33, https://doi.org/10.1016/j.proci.2022.06.001.
[39] R. Schwiedernoch, S. Tischer, C. Correa, O. Deutschmann, Experimental and numerical study on the transient behavior of partial oxidation of methane in a catalytic monolith, Chem. Eng. Sci. 58 (2003) 633–642, https://doi.org/10.1016/S0009-2509(02)00589-4.
[40] O. Deutschmann, S. Tischer, C. Correa, D. Chatterjee, S. Kleditzsch, V. Janardhanan, N. Mladenov, H.D. Minh, H. Karadeniz, M. Hettel, V. Menon, A. Banerjee, H. Goßler, E. Daymo, A.B. Shirsath, DETCHEM Software package (2.8 ed), (2021).
[41] K. Herrera Delgado, L. Maier, S. Tischer, A. Zellner, H. Stotz, O. Deutschmann, Surface reaction kinetics of steam- and CO_2-reforming as well as oxidation of methane over nickel-based catalysts, Catalysts. 5 (2015) 871–904, https://doi.org/10.3390/catal5020871.
[42] M.Y. Sinaki, E.A. Matida, F. Hamdullahpur, Development of a reaction mechanism for predicting hydrogen production from homogeneous decomposition of methane, Int. J. Hydrogen Energy. 36 (2011) 2936–2944, https://doi.org/10.1016/j.ijhydene.2010.12.002.
[43] A.M. Dunker, J.P. Ortmann, Kinetic modeling of hydrogen production by thermal decomposition of methane, Int. J. Hydrogen Energy. 31 (2006) 1989–1998, https://doi.org/10.1016/j.ijhydene.2006.01.013.
[44] B. Zhao, Z. Yang, M.V. Johnston, H. Wang, A.S. Wexler, M. Balthasar, M. Kraft, Measurement and numerical simulation of soot particle size distribution functions in a laminar premixed ethylene-oxygen-argon flame, Combust. Flame. 133 (2003) 173–188, https://doi.org/10.1016/S0010-2180(02)00574-6.
[45] P. Kraus, R.P. Lindstedt, Variational Transition State Theory-Based Surface Chemistry for the $C_2H_6/H_2/O_2$/Pt System, Energy and Fuels. 31 (2017) 2217–2227, https://doi.org/10.1021/acs.energyfuels.6b02189.
[46] Q. Zhu, S.L. Wegener, C. Xie, O. Uche, M. Neurock, T.J. Marks, Sulfur as a selective "soft" oxidant for catalytic methane conversion probed by experiment and theory, Nat. Chem. 5 (2013) 104–109, https://doi.org/10.1038/nchem.1527.
[47] P. Kraus, R.P. Lindstedt, Microkinetic mechanisms for partial oxidation of methane over platinum and rhodium, J. Phys. Chem. c. 121 (2017) 9442–9453, https://doi.org/10.1021/acs.jpcc.7b02397.
[48] H. Stotz, L. Maier, O. Deutschmann, Methane oxidation over palladium: On the mechanism in fuel-rich mixtures at high temperatures, Top. Catal. 60 (2017) 83–109, https://doi.org/10.1007/s11244-016-0717-5.
[49] K. Keller, P. Lott, H. Stotz, L. Maier, O. Deutschmann, Microkinetic modeling of the oxidation of methane over pdo catalysts-towards a better understanding of the water inhibition effect, Catalysts. 10 (2020) 1–21, https://doi.org/10.3390/catal10080922.
[50] F. Gudmundson, J.L. Persson, M. Forsth, F. Behrendt, B. Kasemo, A. Rosen, OH gas phase chemistry outside a Pt catalyst, J. Catal. 179 (1998) 420–430.
[51] A. Kooh, J.L. Dubois, H. Mimoun, C.J. Cameron, Oxidative coupling of methane: maximizing the yield of coupling products under cofeed operating conditions, Catal. Today. 6 (1990) 453–462, https://doi.org/10.1016/0920-5861(90)85039-Q.
[52] K. Takanabe, E. Iglesia, Mechanistic aspects and reaction pathways for oxidative coupling of methane on $Mn/Na_2WO_4/SiO_2$ catalysts, J. Phys. Chem. c. 113 (2009) 10131–10145, https://doi.org/10.1021/jp9001302.
[53] S. Porras, D. Kaczmarek, J. Herzler, S. Drost, M. Werler, T. Kasper, M. Fikri, R. Schießl, B. Atakan, C. Schulz, U. Maas, An experimental and modeling study on the reactivity of extremely fuel-rich methane/dimethyl ether mixtures, Combust. Flame. 212 (2020) 107–122, https://doi.org/10.1016/j.combustflame.2019.09.036.
[54] H. Wang, M. Frenklach, A detailed kinetic modeling study of aromatics formation in laminar premixed acetylene and ethylene flames, Combust. Flame. 110 (1997) 173–221, https://doi.org/10.1016/S0010-2180(97)00068-0.
[55] O. Korup, S. Mavlyankariev, M. Geske, C.F. Goldsmith, R. Horn, Measurement and analysis of spatial reactor profiles in high temperature catalysis research, Chem. Eng. Process. Process Intensif. 50 (2011) 998–1009, https://doi.org/10.1016/j.cep.2011.05.024.